

Concentrated Gaussian curvature in curved creases of actuated spiral nematic solids

Fan Feng¹, Daniel Duffy², John S. Biggins², and Mark Warner^{1,*}

¹*Cavendish Laboratory, University of Cambridge, Cambridge CB3 0HE, United Kingdom*

²*Department of Engineering, University of Cambridge, Cambridge CB2 1PZ, United Kingdom*
**mw141@cam.ac.uk*

February 28, 2025

Abstract

Liquid crystal elastomers/glasses are active materials that can have significant metric change upon stimulation. The local metric change is determined by its director pattern that describes the ordering direction and hence the direction of contraction. We study logarithmic spiral patterns on flat sheets that evolve into cones on deformation, with Gaussian curvature (GC) localized at tips. Such surfaces, Gaussian flat except at their tips, can be combined to give compound surfaces with GC concentrated in lines. We characterize all possible metric-compatible interfaces between two log spiral patterns, specifically where the same metric change occurs on each side. They are classified as hyperbolic-type, elliptic-type, concentric spiral, and continuous-director interfaces. Upon the cone deformations and additional isometries, the actuated interfaces form creases bearing non-vanishing concentrated GC, which is formulated analytically for all cases and simulated numerically for some examples. Analytical calculations and the simulations agree qualitatively well. Furthermore, the relaxation of Gaussian-curved creases is discussed and cantilevers with Gaussian curvature-enhanced strength are proposed. Taken together, our results provide new insights in the study of curved creases, lines bearing GC, and their mechanics arising in actuated liquid crystal elastomers/glasses, and other related active systems.

1 Introduction

Thin and slender structures find wide applications in engineering, ranging from small-scale medical stents [29] to large-scale space structures [39], by forming desired surfaces. The geometry-material-mechanics coupling in these structures has attracted interest in many areas, including the buckling of shells, the crumpling of paper, and the design of active surfaces etc. [3]. Gaussian curvature (GC), defined as the product of the two principal curvatures, is an intrinsic geometrical quantity that plays a crucial role in determining the mechanical behaviour of an elastic surface; for example, the developability of a surface without stretch. Therefore, a method for designing a desired GC is urgently required. GC can be distributed smoothly over surfaces, leading to smooth, curved surfaces

in space. It is well-known from *Gauss’s Theorema Egregium* [22] that isometric deformations are incapable of changing the GC. Deformations that do change GC are hence quite rigid compared with pure bending. Thus, effective non-isometric deformations induced in active materials [28, 30, 33, 34, 36, 15], and in origami/kirigami constructions [14, 6, 7, 9] etc. are employed to achieve non-trivial GC, any blocking of which leads to strong actuation. In this paper, we study active materials, namely liquid crystal elastomers (LCEs) and glasses [54], and examine the GC induced on actuation.

LCEs can have significant shape change determined by their ordering direction, the *director* \mathbf{n} . The shape change can be driven by heat, light, or solvent. The director field is patterned on a two dimensional (2D) sheet. Upon stimulation, LC solid sheets contract by a factor $\lambda < 1$ along the director and elongate by $\lambda^{-\nu}$ along the perpendicular direction, where ν is the *optothermal Poisson ratio*. The deformation is non-isometric and generically induces non-trivial GC [30, 33, 36] and metric change locally. Non-uniform director fields result in non-uniform metric change throughout the pattern, and therefore the coupled mechanical behavior becomes sophisticated. This metric-driven paradigm has been termed “metric mechanics” [52] and can be used to design targeted, three-dimensional shapes actuated from a prescribed 2D (usually smooth) director pattern [30, 1, 36, 53, 2, 23]. For example, a circular pattern and its actuated state, cones [Fig. 1(a)], have been used to design heavy lifters that experimentally can lift thousands of times their own mass through strokes that are hundreds of times their own thickness [51, 55]. Fundamentally, the strength of the lifter is enhanced by the tips of cones, which are point defects of concentrated GC preventing the lifter from being flattened.

Beyond smooth director patterns and point defects, we are interested in “interfaces” formed at curves separating two patterns. To form a geometrically-consistent deformed configuration with interfaces, the deformations on the two sides have to be different, but obey the so-called geometrical compatibility (or rank-1 compatibility [5]) condition to ensure the continuity of the configuration across the interface. The study of compatible interfaces can be traced back to martensitic phase transformations in crystals with straight-line interfaces [5, 46], more recently in helical structures with curved interfaces [21, 19], and straight-fold/curved-fold origami [17, 48, 10, 11, 24, 42]. Examples in LCEs include the straight-line interface between piecewise constant director patterns [31, 41, 40] and the hyperbolic/elliptical interfaces between circular patterns [32, 18] (see Figs. 1(b)-(d)). These examples of non-isometric origami have interfaces that are geometrically consistent, before and after deformation. For example, in Figs. 1(b–d), the actuated interfaces under the conical deformations from the different patterns that meet are identical and fit together at the fold without the need for further (isometric) shape change. We name this particular scenario *conical consistency*.

However, the actuated state can be further deformed isometrically. Like in classical, isometric curved-fold origami [20, 13, 4, 8], the additional isometric deformation preserves the GC and the geodesic curvature distributed along the deformed interface. This constraint links the deformed interface and the surfaces on two sides via the crease’s opening angle which can be calculated from the total curvature and geodesic curvature of the interface. Usually these additional isometric deformations are sophisticated and can not be determined analytically, but they do occur in soft materials such as paper and LCEs. Allowing such arbitrary additional isometric deformations, *metric compatibility* is employed. That is, the metric changes at the interface induced by the two sides need to be identical. As a result, the deformed interfaces from the two sides have the same local arc length. Interfaces that satisfy metric compatibility and have the same deformed local arc

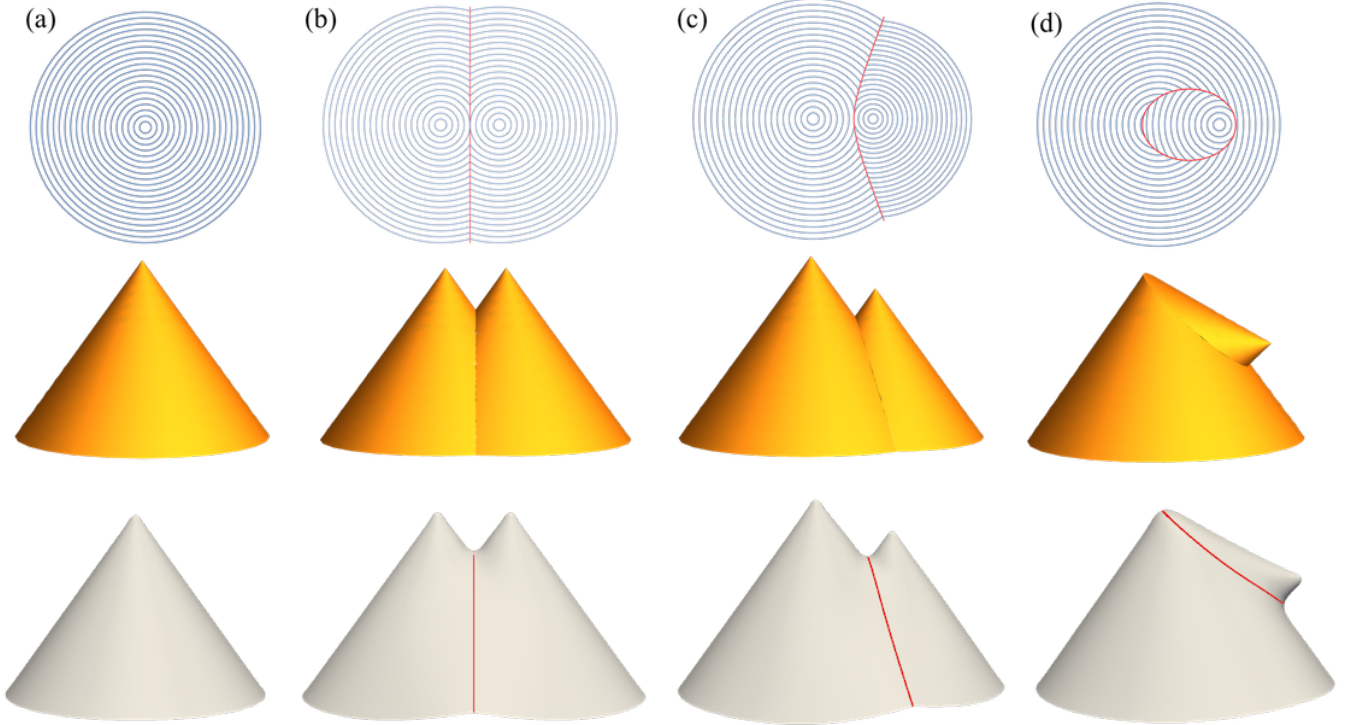


Figure 1: The circular director patterns (top), the theoretical actuated configurations (middle), and the simulated configurations (bottom). (a) A circular pattern and its actuated state, a cone. (b) Straight-line interface between two circular patterns that bisects the line joining their centers. The actuated cones have equal height and parallel cone axes. (c) Hyperbolic interface between two circular patterns. The interface is not bisecting and hence the actuated cones have different heights, but parallel cone axes. (d) Elliptical interface between two circular patterns. The actuated cones have nonparallel cone axes. The deformed interfaces are geometrically consistent, that is, they have the same shape under either conical deformation.

length are named metric-compatible interfaces, which are the focus of this paper.

In this paper, we move beyond the above conically-consistent, non-isometric origami in Fig. 1 and study both the metric-compatible interfaces and the post-actuation isometries in LCEs. In particular, we study logarithmic spiral director patterns, which cause sheets to evolve into cones in 3D under so-called *cone deformations*. Similar to those from circular patterns, cones actuated from spiral patterns have a point source of positive GC localized at the tip, with a value of $2\pi(1 - \sin \varphi)$ calculated from the angular deficit, where φ is the cone angle [18]. We are interested in GC concentrated in activated tips and curved creases, in systems that are otherwise Gaussian flat and convenient to solve. In contrast with that of circular patterns, the cone deformation of spiral patterns contains a non-uniform rotation term that causes conical inconsistency of the deformed interface. The metric-compatible interfaces between spiral patterns are also more complicated, while in circular patterns the interfaces are simply hyperbolae or ellipses [18]. Fortunately, one can employ elliptic coordinates to derive the analytical forms for all possible metric-compatible interfaces between two spiral patterns. We characterize these interfaces into four types: hyperbolic-type, elliptic-type, continuous-director, and concentric spiral interfaces. These interfaces generically

carry non-trivial GC, fundamentally because the deformation from 2D to 3D is non-isometric. The GC distributed along a curve parallel or perpendicular to the director in a general director pattern is given in a recent work [15], by applying the Gauss-Bonnet theorem locally to a loop containing the curve. Here we employ the same approach and further derive formulae for the GC concentrated along a metric-compatible interface between two director patterns.

As yet we have no theoretical tools to compute the post-actuation isometries that can resolve the conical inconsistency for actuated spiral patterns, so we instead present simulations that provide this resolution. Our numerical approach models a thin patterned LCE sheet as a 2D surface, assigns it an elastic energy containing both stretch and bend terms, and minimizes that energy to find an equilibrium state. The simulated post-actuation deformations are not exact isometries, but we quantify the degree of non-isometry in Section 3 and find it to be negligibly small, apart from localized “blunting” deformations that regularize any singular curvature encoded in the director pattern.

The paper is organized as follows. In Section 2, we study isolated logarithmic spiral patterns and derive the explicit cone deformations that map the reference domain to actuated cones. In Section 3, all possible metric-compatible interfaces between two spiral patterns are characterized. The disconnected actuated states under the separate cone deformations, and the connected, continuous simulated configurations are presented. In Section 4, we discuss the conical inconsistency under cone deformations and argue that additional isometries, which preserve the GC, are needed to form continuous, actuated configurations. In Section 5, we provide three methods for computing the analytical GC concentrated along the actuated interface. Simulations and analytical results are compared qualitatively for two examples, and agree well. In the discussion section, we propose a design of LCE cantilevers with their strength potentially enhanced by concentrated GC, and discuss the relaxation of non-isometric folds. Our findings provide insights into curved creases, lines of concentrated GC, and the coupled mechanics of spiral director patterns and of anticipated general patterns in active systems.

2 Logarithmic spiral director field and cone deformation

2.1 Reference domain

Let $\{\mathbf{e}_1, \mathbf{e}_2, \mathbf{e}_3\}$ be the orthonormal basis of the Cartesian coordinates. Consider a general director field $\mathbf{n}(x, y) = n_1(x, y)\mathbf{e}_1 + n_2(x, y)\mathbf{e}_2$ at the position $(x, y) \in \mathcal{D} \subset \mathbb{R}^2$ satisfying $|\mathbf{n}(x, y)| = 1$, where \mathcal{D} is the domain of the director field. Logarithmic spiral director patterns are in the class of circularly symmetric patterns – the GC on actuation of such patterns has been investigated in [30, 1, 36] who proved that spiral patterns deform into cones. It is convenient to use the polar coordinates (r, θ) to denote the position (x, y) in Cartesian coordinates, i.e., $(x, y) = (r \cos \theta, r \sin \theta)$. The components $n_1(x, y)$ and $n_2(x, y)$ for spiral pattern have the forms

$$\begin{aligned} n_1(x, y) &= \bar{n}_1(r, \theta) = \cos(\theta + \alpha), \\ n_2(x, y) &= \bar{n}_2(r, \theta) = \sin(\theta + \alpha), \end{aligned} \tag{1}$$

$$\mathbf{n}(r, \theta) = \cos(\theta + \alpha)\mathbf{e}_1 + \sin(\theta + \alpha)\mathbf{e}_2, \tag{2}$$

where $\alpha \in (-\pi/2, 0) \cup (0, \pi/2)$ is a constant angle between the tangent of the spiral passing through (x, y) and the radial direction (see Fig. 2(a)). Here we carefully choose the domain of α to exclude

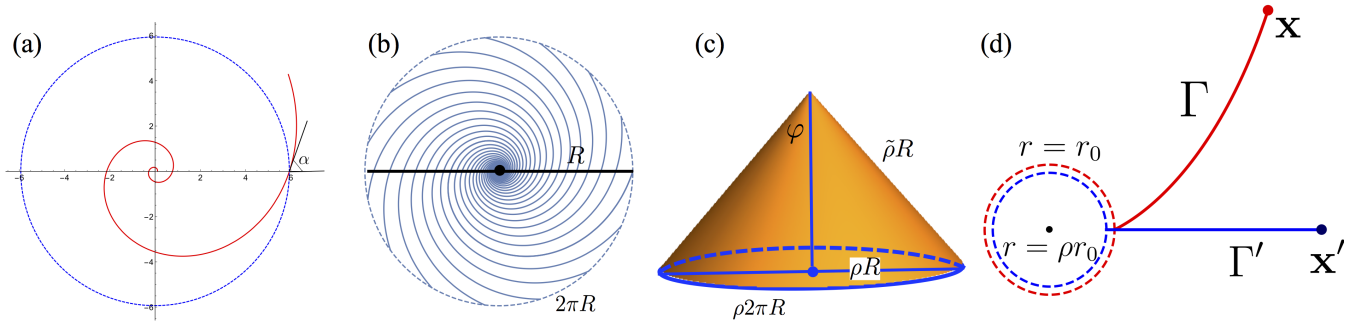


Figure 2: (a) A logarithmic spiral curve $r(\theta) = r_0 \exp\left(\frac{\theta}{\tan \alpha}\right)$ in red with $r_0 = 0.1$ and $\alpha = \pi/2.5$. The angle between the tangent of the curve (solid, red) and the radial direction is a constant angle α . (b) A logarithmic director pattern in \mathbb{R}^2 with radius R . (c) A cone evolved from the patterned reference state has the slant height $\tilde{\rho}R$, base radius ρR , and cone angle φ determined by the cone deformation Eq. (13). The coefficients $\tilde{\rho}$ and ρ are given in the text. (d) The proto-radius Γ (red) is deformed to the actual radius Γ' (blue) upon actuation. The actual radius is illustrated by projecting onto \mathbb{R}^2 . Without loss of generality, we assume the $r = r_0$ circle remains unrotated but has a rescaled radius after actuation.

two degenerate cases: the radial pattern with $\alpha = 0$ and the circular pattern with $\alpha = \pm\pi/2$. These two degenerate cases make some of our formulae not well-defined and thus will be treated separately. The circular pattern has been extensively studied in [36, 35, 18], and will also be discussed in this paper, as a special case of the spiral pattern. For smaller α , and in particular $\alpha = 0$ (radial director), actuation is to an anti-cone where circumferences are long relative to their radii and ruffled shapes with negative localized GC result [30].

The spiral pattern satisfying Eq. (1) is constructed in the following way. Firstly the single spiral [Fig. 2(a)] is of the form

$$r(\theta) = r_0 \exp\left(\frac{\theta}{\tan \alpha}\right) \quad (3)$$

in polar coordinates, where r_0 defines the reference radius for $\theta = 0$. The director on the spiral is defined as its unit tangent. One can easily confirm that the director satisfies Eq. (2) by this definition. The spiral director pattern \mathcal{D} (initially assumed to be infinite) in Fig. 2(b) is constructed by applying a continuous rotation to a single spiral, say,

$$\mathcal{D} = \left\{ r_0 \exp\left(\frac{\theta}{\tan \alpha}\right) \mathbf{R}(\xi) \mathbf{e}_r : \xi \in [0, 2\pi), \theta \in \mathbb{R} \right\}, \quad (4)$$

where $\mathbf{R}(\cdot) = \cos(\cdot)(\mathbf{e}_1 \otimes \mathbf{e}_1 + \mathbf{e}_2 \otimes \mathbf{e}_2) + \sin(\cdot)(-\mathbf{e}_1 \otimes \mathbf{e}_2 + \mathbf{e}_2 \otimes \mathbf{e}_1)$ is a rotation in \mathbb{R}^2 , and $\mathbf{e}_r = \cos \theta \mathbf{e}_1 + \sin \theta \mathbf{e}_2$ is the radial direction. The domain \mathcal{D} is well defined in the sense that each point with $r \neq 0$ in \mathbb{R}^2 corresponds to one and only one pair of (ξ, θ) in the domain defined in (4). To achieve a finite domain of director, for example a circular plate with radius $R > r_0$, one has to truncate θ by $\theta \in [0, \theta_0]$ for $\tan \alpha > 0$ or $\theta \in [\theta_0, \infty)$ for $\tan \alpha < 0$, where $\theta_0 = \tan \alpha \ln(R/r_0)$.

2.2 Cone deformation

The spiral pattern with radius R illustrated in Fig. 2(b) will deform into a cone in Fig. 2(c) or an anticone [30] upon stimulation, depending on the material parameters and the spiral constant α . It is shown in [31, 30, 36, 35] that the spiral pattern results in a cone or an anti-cone depending on whether the spiral constant α is greater than or less than the threshold angle $\alpha_c = \arcsin\left(\sqrt{\frac{\lambda^{-2\nu} - \lambda^{1-\nu}}{\lambda^{-2\nu} - \lambda^2}}\right)$. The spontaneous deformation gradient associated with the director \mathbf{n} has the symmetric form

$$\mathbf{U}_{\mathbf{n}} = \lambda \mathbf{n} \otimes \mathbf{n} + \lambda^{-\nu} \mathbf{n}^{\perp} \otimes \mathbf{n}^{\perp}, \quad (5)$$

where $\mathbf{n}^{\perp} = \mathbf{R}(\pi/2)\mathbf{n}$ is perpendicular to \mathbf{n} in the plane of the sheet and the tensor component $(\mathbf{n} \otimes \mathbf{n})_{ij} = \mathbf{n}_i \mathbf{n}_j$. Under $\mathbf{U}_{\mathbf{n}}$, the pattern has a contraction $\lambda < 1$ along \mathbf{n} and an elongation $\lambda^{-\nu}$ along \mathbf{n}^{\perp} with the optothermal Poisson ratio ν .

We focus on the cone case here and revisit the metric tensor argument in [36] to derive an explicit deformation that maps the material point on the reference director pattern to the corresponding point on the actuated cone.

Recalling the argument in [36], the components of the metric tensor \mathbf{a} for an actuated spiral pattern in polar coordinates are

$$\begin{aligned} a_{rr} &= \lambda^2 + (\lambda^{-2\nu} - \lambda^2) \sin^2 \alpha, \\ a_{r\theta} &= a_{\theta r} = -r(\lambda^{-2\nu} - \lambda^2) \sin(2\alpha), \\ a_{\theta\theta} &= r^2[\lambda^{-2\nu} - (\lambda^{-2\nu} - \lambda^2) \sin^2 \alpha]. \end{aligned} \quad (6)$$

We define proto-radii Γ in Fig. 2(d) on the reference domain as curves that deform to be actual radii Γ' after actuation [35]. The proto-radii are indicators of how much rotation takes place on actuation, and it is rotation that gives the difficulty in fitting the actuated cones together at their interface. By circular symmetry, the deformation takes circles into circles. Let Γ have the parametric form $(r(s), \theta(s))$ in polar coordinates. Then the tangents of Γ and circles have to obey

$$\mathbf{t}_1 \cdot \mathbf{a} \cdot \mathbf{t}_2 = 0, \quad (7)$$

where $\mathbf{t}_1 = (0, 1)$ is the tangent to a circle and $\mathbf{t}_2 = (dr/ds, d\theta/ds)$ is the tangent to Γ . Solving Eq. (7), one can obtain the expression of the proto-radii Γ as

$$r(\theta) = r_0 \exp\left(\frac{\theta}{b}\right), \quad (8)$$

where $b = \frac{(1-\lambda^{2(1+\nu)}) \cot \alpha}{\lambda^{2(1+\nu)} + \cot^2 \alpha}$. Without loss of generality, we assume the circle $r = r_0$ is unrotated after actuation. Then the material point \mathbf{x} in Fig. 2(c) is deformed to \mathbf{x}' with a relative rotation $-b \ln\left(\frac{r}{r_0}\right)$, where $r = |\mathbf{x}|$.

As illustrated in Fig. 2(c), the deformed cone has a rescaled base radius ρr and a rescaled slant height $\tilde{\rho} r$. The coefficients ρ and $\tilde{\rho}$ are

$$\begin{aligned} \rho &= \sqrt{\lambda^{-2\nu} - (\lambda^{-2\nu} - \lambda^2) \sin^2 \alpha}, \\ \tilde{\rho} &= \frac{\lambda^{1-\nu}}{\sqrt{\lambda^{-2\nu} - (\lambda^{-2\nu} - \lambda^2) \sin^2 \alpha}}. \end{aligned} \quad (9)$$

These scaling coefficients can be calculated by the metric change along the proto-radii and the circumference:

1. The circumference of the deformed cone, which accordingly defines the in-space radius, is

$$\rho 2\pi R = \int_0^{2\pi} \sqrt{a_{\theta\theta}(R)} d\theta = 2\pi R \sqrt{\lambda^{-2\nu} - (\lambda^{-2\nu} - \lambda^2) \sin^2 \alpha}; \quad (10)$$

2. The proto-radii emanating from the origin give radii upon actuation of in-material length

$$\tilde{\rho} R = \int_0^R \sqrt{a_{rr} + 2a_{r\theta} dr/d\theta + a_{\theta\theta} (d\theta/dr)^2} dr = \frac{\lambda^{1-\nu}}{\sqrt{\lambda^{-2\nu} - (\lambda^{-2\nu} - \lambda^2) \sin^2 \alpha}} R. \quad (11)$$

The cone angle φ is then given by the ratio of radii as

$$\varphi = \arcsin(\rho/\tilde{\rho}) = \arcsin[\lambda^{-1-\nu} - (\lambda^{-1-\nu} - \lambda^{1+\nu}) \sin^2 \alpha]. \quad (12)$$

According to the previous discussion, we next define the *cone deformation* that encodes the rotation of the in-material point and maps the reference pattern to the corresponding cone surface. For a spiral director pattern occupying the reference region $\mathcal{D} = \{(r \cos \theta, r \sin \theta) : r \in (0, R), \theta \in (0, 2\pi]\}$ with the spiral constant α , we define the cone deformation $\mathbf{y}_\alpha : \mathcal{D} \rightarrow \mathbb{R}^3$ as

$$\mathbf{y}_\alpha(\mathbf{r}) = \rho r \left[\mathbf{R}_{\mathbf{e}_3} \left(-b \ln \frac{r}{r_0} \right) \mathbf{e}_r - \cot \varphi \mathbf{e}_3 \right], \quad \mathbf{r} \in \mathcal{D}, \quad (13)$$

where R is the radius of the reference domain (see Fig. 2(b)), $\mathbf{r} = (r \cos \theta, r \sin \theta)$, $\mathbf{e}_r = \cos \theta \mathbf{e}_1 + \sin \theta \mathbf{e}_2$, $\rho = \sqrt{\lambda^2 \sin^2 \alpha + \lambda^{-2\nu} \cos^2 \alpha}$, $b = \frac{(1-\lambda^{2(1+\nu)}) \cot \alpha}{\lambda^{2(1+\nu)} + \cot^2 \alpha}$, $\mathbf{R}_{\mathbf{e}_3}(\cdot) = \cos(\cdot)(\mathbf{e}_1 \otimes \mathbf{e}_1 + \mathbf{e}_2 \otimes \mathbf{e}_2) + \sin(\cdot)(-\mathbf{e}_1 \otimes \mathbf{e}_2 + \mathbf{e}_2 \otimes \mathbf{e}_1) + \mathbf{e}_3 \otimes \mathbf{e}_3$ is a rotation with axis \mathbf{e}_3 , and the cone angle φ is given by (12). For circular patterns with $\alpha = \pm\pi/2$, the cone deformation degenerates to

$$\mathbf{y}_c(\mathbf{r}) = \rho r (\mathbf{e}_r - \cot \varphi \mathbf{e}_3), \quad (14)$$

where $\rho = \lambda$ and $\varphi = \arcsin(\lambda^{1+\nu})$, with no rotation ($b = 0$), by substituting $\alpha = \pm\pi/2$.

3 Metric-compatible interfaces between two spiral patterns

Now we consider two director patterns separated by an interface. Generally, the actuated interfaces from the two patterns are intrinsically different – the local metric changes of the interface from two patterns are not equal and therefore no isometry can stitch these two patterned pieces together at common interface isometrically achieved from the original two, deformed interfaces. Incompatibility in metric (for example metrics induced by swelling [27]) usually leads to complex shape change coupled with mechanics, which is beyond the scope of this paper. To construct a non-isometric origami, we focus our attention on a metric-compatible interface that has the same stretches along its length induced by actuating the two patterns. A canonical example is the interface between circular director patterns [Fig. 1]. In [18], it is found that the metric-compatible interface evolves

into a conically consistent interface in 3D, and then the actuated configuration is simply the combination of cones with the same cone angles, and no rotations are involved. Since the metric change induced by inhomogeneous director patterns is non-trivial, the actuated interface carries non-trivial, concentrated GC.

Looking beyond circular patterns, we now study the metric-compatible interfaces between two spiral patterns. The metric compatibility condition, as discussed in [18], ensures that the interfaces arising from actuation according to the two respective patterns have the same metric locally. The metric compatibility derived from the metric change has the following equivalent forms, using the deformation gradient of Eq. (5):

$$|\mathbf{U}_{\mathbf{n}_1} \mathbf{t}| = |\mathbf{U}_{\mathbf{n}_2} \mathbf{t}| \Leftrightarrow \mathbf{t} \cdot \mathbf{a}_1 \cdot \mathbf{t} = \mathbf{t} \cdot \mathbf{a}_2 \cdot \mathbf{t} \Leftrightarrow (\mathbf{n}_1 \cdot \mathbf{t})^2 = (\mathbf{n}_2 \cdot \mathbf{t})^2, \quad (15)$$

where \mathbf{t} is the unit tangent to the interface, $\mathbf{n}_1, \mathbf{n}_2$ are directors on two sides of the interface, and $\mathbf{a}_i = \mathbf{U}_{\mathbf{n}_i}^T \mathbf{U}_{\mathbf{n}_i}$ is the metric tensor for $i = 1, 2$. Now we explicitly and exhaustively characterize all possible metric-compatible interfaces between two spiral patterns, by solving the metric compatibility (15) for \mathbf{n}_1 and \mathbf{n}_2 belonging to two spiral patterns. Suppose two spiral patterns centered at $\mathbf{c}_1 = (-c, 0)$ and $\mathbf{c}_2 = (c, 0)$ are given by

$$\begin{aligned} \mathcal{D}_1 &= \left\{ r_0 \exp\left(\frac{\theta}{\tan \alpha_1}\right) \mathbf{R}(\xi) \mathbf{e}_r - c \mathbf{e}_1 : \xi \in [0, 2\pi), \theta \in \mathbb{R} \right\}, \\ \mathcal{D}_2 &= \left\{ r_0 \exp\left(\frac{\theta}{\tan \alpha_2}\right) \mathbf{R}(\xi) \mathbf{e}_r + c \mathbf{e}_1 : \xi \in [0, 2\pi), \theta \in \mathbb{R} \right\}. \end{aligned} \quad (16)$$

Let $\gamma(s)$ be a parametric form of the curved interface separating \mathcal{D}_1 and \mathcal{D}_2 . The unit tangent is then $\mathbf{t}(s) = \gamma'(s)/|\gamma'(s)|$. In the following we drop explicitly displaying s -dependence to abbreviate notations, and \mathbf{t} is not generally a constant vector.

We will prove that the solution to Eq. (15) essentially has four situations:

- *Hyperbolic-type interface.* If $c \neq 0$ and $\mathbf{n}_1 \neq \pm \mathbf{n}_2$, one solution to (15) is $\mathbf{t} \cdot \mathbf{n}_1 = \mathbf{t} \cdot \mathbf{n}_2$. In this case, the tangent \mathbf{t} bisects the two directors \mathbf{n}_1 and \mathbf{n}_2 .
- *Elliptic-type interface.* The other solution for the case $c \neq 0$ and $\mathbf{n}_1 \neq \pm \mathbf{n}_2$ is $\mathbf{t} \cdot \mathbf{n}_1 = -\mathbf{t} \cdot \mathbf{n}_2$. In this case, the tangent \mathbf{t} is perpendicular to the bisector of \mathbf{n}_1 and \mathbf{n}_2 .
- *Continuous-director interface.* The directors on two sides of the interface are parallel, i.e., $\mathbf{n}_1 = \pm \mathbf{n}_2$. Then Eq. (15) holds trivially.
- *Concentric spiral interface.* If $c = 0$, the two spiral patterns have the same center. We find that the metric-compatible interface between them is a logarithmic spiral with the same center, but different spiral constant α , or the interface degenerates to a radial line or a circle.

These four types of interfaces are named according to their geometrical features on the reference domain which will be discussed in detail in the following subsections. Before heading to theoretical results and simulations, we elucidate some settings throughout the paper:

- The material constants $\lambda = 0.7$ and $\nu = 0.5$ are chosen as typical of incompressible elastomers.
- For simulations, the spiral patterns have the centers at $(-2, 0)$ and $(2, 0)$, if they are not concentric.

- The boundary of the reference domain is a circle with radius $R = 8$ if not additionally noted.
- The left/right actuated configuration (e.g. the yellow conical configurations in Fig. 4) is obtained by cutting along the interface and then applying the corresponding cone deformation to the left/right pattern separately.

Our simulations were conducted with Morphoshell, a bespoke “active-shell” code. For full details see Ref. [15]. The numerical approach models a thin sheet of incompressible Neo-Hookean elastomer as a 2D surface, assigns an elastic energy to that surface, and minimises that energy to find equilibrium configurations. The energy penalises both stretch (deviations from the “programmed” metric in Eq. (6)), and bend. Taking the reference-state thickness of the sheet to be h , the stretch and bend energies are $\propto h$ and $\propto h^3$ respectively, as is usual for a thin shell. Thus, for suitably small h the stretch energy dominates, and the activated surface approaches an isometry of the programmed metric.

The programmed metrics considered in this work generically encode singular curvature at spiral centers and along interfaces. Thus at any non-zero h there are localized regions around these features which are significantly non-isometric, and exhibit only finite curvature, thereby relieving a singular bend energy at the cost of some stretch energy. This effect is the cause of the visible “blunting” of all simulated interfaces and cone tips. In the $h \rightarrow 0$ limit, the domination of stretch over bend ensures that the size of these blunted regions tends to zero, with the local curvature diverging accordingly.

To locally quantify the degree of non-isometry, we use the root mean square of the two principal strains of the deformed surface, relative to an isometry of the programmed metric. Away from the expected ‘blunted’ regions, the characteristic size of this strain measure was $\epsilon \lesssim 0.003$ in all simulations, confirming that our simulated surfaces are indeed near-isometries of the programmed metric. This in turn provides strong evidence that even when the two activated surfaces formed on either side of a metric-compatible interface are conically inconsistent, they can nonetheless be ‘fitted together’ isometrically.

Finally, we note that some of the simulated surfaces, although entirely physical, may only be local energy minima because the surfaces are multistable in general.

3.1 Hyperbolic-type and elliptic-type interfaces

We employ elliptic coordinates to calculate the hyperbolic-type and elliptic-type interfaces. As illustrated in Fig. 3(a), two spirals $\Gamma_1 \in \mathcal{D}_1$ and $\Gamma_2 \in \mathcal{D}_2$ from the two patterns intersect at the point

$$\mathbf{x} = (x(u, v), y(u, v)) = c(\cosh u \cos v, \sinh u \sin v), \quad (17)$$

where $u \geq 0$, $v \in [0, 2\pi)$, and two spiral centers are located at $(-c, 0)$ and $(c, 0)$. The curves of constant u form ellipses and the curves of constant v form hyperbolae, as shown in Fig. 3(a). For $\mathbf{n}_1 \neq \pm \mathbf{n}_2$ and $c \neq 0$, metric-compatible interfaces are either hyperbolic-type, I_1 , with tangent \mathbf{t} bisecting \mathbf{n}_1 and \mathbf{n}_2 , or elliptic-type, I_2 , with tangent \mathbf{t}' bisecting $-\mathbf{n}_1$ and \mathbf{n}_2 . Following the geometry in Fig. 3(a), elliptical-hyperbolic systems have the properties:

$$\mathbf{r}_1 = \mathbf{x} - \mathbf{c}_1, \quad |\mathbf{r}_1| = c(\cos v + \cosh u), \quad \mathbf{n}_1 = \mathbf{R}(\alpha_1) \frac{\mathbf{r}_1}{|\mathbf{r}_1|},$$

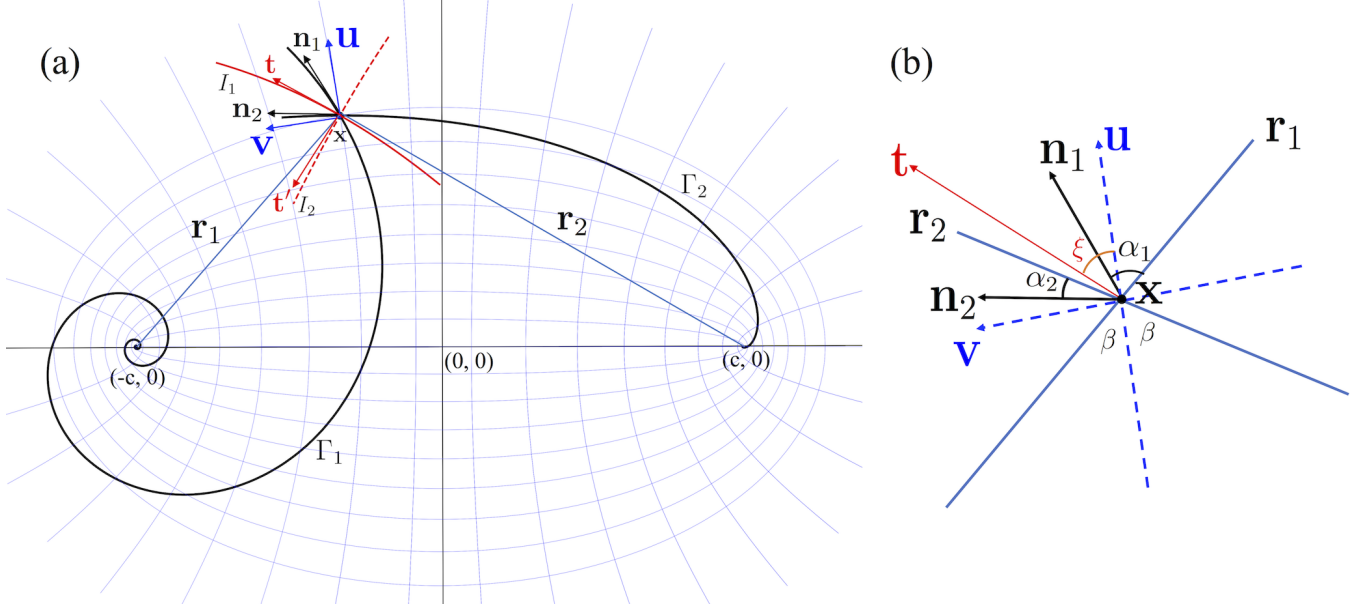


Figure 3: (a) Metric-compatible interfaces (red) between two spiral patterns in elliptic coordinates. Two spirals Γ_1 and Γ_2 centered at $\mathbf{c}_1 = (-c, 0)$ and $\mathbf{c}_2 = (c, 0)$ intersect at \mathbf{x} . The directors at \mathbf{x} are \mathbf{n}_1 and \mathbf{n}_2 . Two interfaces I_1 and I_2 passing through \mathbf{x} have tangents \mathbf{t} bisecting \mathbf{n}_1 and \mathbf{n}_2 , and \mathbf{t}' bisecting $-\mathbf{n}_1$ and \mathbf{n}_2 . The vectors \mathbf{u} and \mathbf{v} (blue) are the tangents along the u -line and v -line that pass through \mathbf{x} . The vectors \mathbf{r}_1 and \mathbf{r}_2 point from the spiral centers \mathbf{c}_1 and \mathbf{c}_2 to \mathbf{x} . These vectors are given explicitly in Eq. (18). (b) Illustration of angles between the vectors. \mathbf{n}_i is obtained by rotating $\mathbf{r}_i/|\mathbf{r}_i|$ counterclockwise by an angle α_i , for $i = 1, 2$. By properties of elliptical coordinates (a proof is given in the text), the vector \mathbf{u} bisects \mathbf{r}_1 and \mathbf{r}_2 with angle β , say. The angle ξ between \mathbf{t} and \mathbf{u} is $\xi = \frac{\alpha_1 + \alpha_2}{2}$ (see text).

$$\mathbf{r}_2 = \mathbf{x} - \mathbf{c}_2, \quad |\mathbf{r}_2| = c(-\cos v + \cosh u), \quad \mathbf{n}_2 = \mathbf{R}(\alpha_2) \frac{\mathbf{r}_2}{|\mathbf{r}_2|},$$

$$\mathbf{u} = \frac{\partial \mathbf{x}}{\partial u} = c(\cos v \sinh u, \sin v \cosh u), \quad \mathbf{v} = \frac{\partial \mathbf{x}}{\partial v} = c(-\sin v \cosh u, \cos v \sinh u). \quad (18)$$

Assume the interface is described by $f(x(u, v), y(u, v)) = 0$. Differentiating f yields

$$(\mathbf{t}^\perp \cdot \mathbf{u})du + (\mathbf{t}^\perp \cdot \mathbf{v})dv = 0, \quad (19)$$

where $\mathbf{t}^\perp = (\frac{\partial f}{\partial x}, \frac{\partial f}{\partial y}) / |(\frac{\partial f}{\partial x}, \frac{\partial f}{\partial y})|$ is the unit normal to the interface. The unit tangent is given by $\mathbf{t} = (-\frac{\partial f}{\partial y}, \frac{\partial f}{\partial x}) / |(-\frac{\partial f}{\partial y}, \frac{\partial f}{\partial x})|$ satisfying $\mathbf{t} \cdot \mathbf{t}^\perp = 0$. We discuss compatibility solutions $\mathbf{t} \cdot \mathbf{n}_1 = \mathbf{t} \cdot \mathbf{n}_2$ and $\mathbf{t} \cdot \mathbf{n}_1 = -\mathbf{t} \cdot \mathbf{n}_2$ for hyperbolic-type and elliptic-type interfaces respectively¹.

Hyperbolic-type interface. For $\mathbf{n}_1 \cdot \mathbf{t} = \mathbf{n}_2 \cdot \mathbf{t}$ and $\mathbf{n}_1 \neq \pm \mathbf{n}_2$, we have two solutions for \mathbf{t} : $\mathbf{t} = \pm \frac{\mathbf{n}_1 + \mathbf{n}_2}{|\mathbf{n}_1 + \mathbf{n}_2|}$, and choose the “+” solution $\mathbf{t} = \frac{\mathbf{n}_1 + \mathbf{n}_2}{|\mathbf{n}_1 + \mathbf{n}_2|}$. The “-” solution inverts the tangent \mathbf{t} to $-\mathbf{t}$

¹Changing α_1 to $\alpha_1 \pm \pi$ or α_2 to $\alpha_2 \pm \pi$ will invert one of the directors and result in the exchange of hyperbolic-type and elliptic-type interfaces, while preserving the two spiral patterns. The previous bisector of the directors is then changed to the orthogonal dual of the bisector of the new directors. We use this fact in Figs. 4(c)(d) to unify the features of the interfaces in the same column.

and gives the same curve. Then $\mathbf{t}^\perp = \frac{-\mathbf{n}_1 + \mathbf{n}_2}{|\mathbf{n}_1 + \mathbf{n}_2|}$. Substituting \mathbf{t}^\perp in terms of \mathbf{n}_1 and \mathbf{n}_2 into (19), by direct calculation we have the differential equation for u and v :

$$\frac{dv}{du} = \tan \frac{\alpha_1 + \alpha_2}{2}, \quad (20)$$

which yields

$$v(u) = u \tan \frac{\alpha_1 + \alpha_2}{2} + v_0. \quad (21)$$

Eq. (20) can also be obtained by a more intuitive geometrical approach. In elliptic coordinates, \mathbf{u} bisects \mathbf{r}_1 and \mathbf{r}_2 as seen by checking $\mathbf{u} \cdot \mathbf{r}_1/|\mathbf{r}_1| = \mathbf{u} \cdot \mathbf{r}_2/|\mathbf{r}_2|$. We denote the angle between \mathbf{r}_1 and \mathbf{u} by β , as illustrated in Fig. 3(b). Since \mathbf{t} bisects \mathbf{n}_1 and \mathbf{n}_2 , then the angle between \mathbf{t} and \mathbf{n}_1 is $(2\beta - \alpha_1 + \alpha_2)/2$. The angle ξ between \mathbf{t} and \mathbf{u} is $\xi = (2\beta - \alpha_1 + \alpha_2)/2 + \alpha_1 - \beta = (\alpha_1 + \alpha_2)/2$, which is a constant. As a consequence, the differential equation (20) for u and v holds.

Finally, the interface $\mathbf{x}(u) = (x(u), y(u))$ is of the form

$$\begin{cases} x(u) = c \cosh u \cos \left(u \tan \frac{\alpha_1 + \alpha_2}{2} + v_0 \right) \\ y(u) = c \sinh u \sin \left(u \tan \frac{\alpha_1 + \alpha_2}{2} + v_0 \right) \end{cases}. \quad (22)$$

Notice that $(x(0), y(0)) = c(\cos v_0, 0)$. Then v_0 is determined by the intersection between the interface and the horizontal axis.

Elliptic-type interface. For $\mathbf{n}_1 \cdot \mathbf{t}' = -\mathbf{n}_2 \cdot \mathbf{t}'$ and $\mathbf{n}_1 \neq \pm \mathbf{n}_2$, we have two solutions for \mathbf{t}' : $\mathbf{t}' = \pm \frac{-\mathbf{n}_1 + \mathbf{n}_2}{|\mathbf{n}_1 + \mathbf{n}_2|}$. Again, we choose the “+” solution, i.e., $\mathbf{t}' = \frac{-\mathbf{n}_1 + \mathbf{n}_2}{|\mathbf{n}_1 + \mathbf{n}_2|}$. Following exactly the same calculations as in the hyperbolic-type interface case, or simply replacing $\frac{\alpha_1 + \alpha_2}{2}$ in Eq. (20) by $\frac{\alpha_1 + \alpha_2}{2} + \pi/2$, we have

$$\frac{du}{dv} = -\tan \frac{\alpha_1 + \alpha_2}{2} \quad (23)$$

for this case, which yields

$$u(v) = -v \tan \frac{\alpha_1 + \alpha_2}{2} + u_0. \quad (24)$$

Thus the interface $\mathbf{x}(v) = (x(v), y(v))$ is of the form

$$\begin{cases} x(v) = c \cosh \left(-v \tan \frac{\alpha_1 + \alpha_2}{2} + u_0 \right) \cos v \\ y(v) = c \sinh \left(-v \tan \frac{\alpha_1 + \alpha_2}{2} + u_0 \right) \sin v \end{cases}. \quad (25)$$

Notice that $(x(0), y(0)) = c(\cosh u_0, 0)$ and thus u_0 is determined by the intersection between the interface and the horizontal axis.

Examples of hyperbolic-type and elliptic-type interfaces. The appearances of the interfaces with analytical forms (22) and (25) highly depend on the parameters $\alpha_1, \alpha_2, u_0, v_0$. Despite having analytical forms, generically the interfaces are sophisticated curves with no symmetries. Notice that hyperbolic-type and elliptic-type interfaces exist in pairs. Here we provide two general cases in Figs. 4(a)(b), and highlight some examples with special α_1 and α_2 in Figs. 4(c)-(f). Fig. 4(a) shows the hyperbolic-type interface between a spiral pattern with $\alpha_1 = 5\pi/12$ and a circular pattern with $\alpha_2 = -\pi/2$. One can clearly see that the tangent of the interface bisects the directors where they meet. Fig. 4(b) shows the elliptic-type interface between these two patterns. Figs. 4(c)(d)

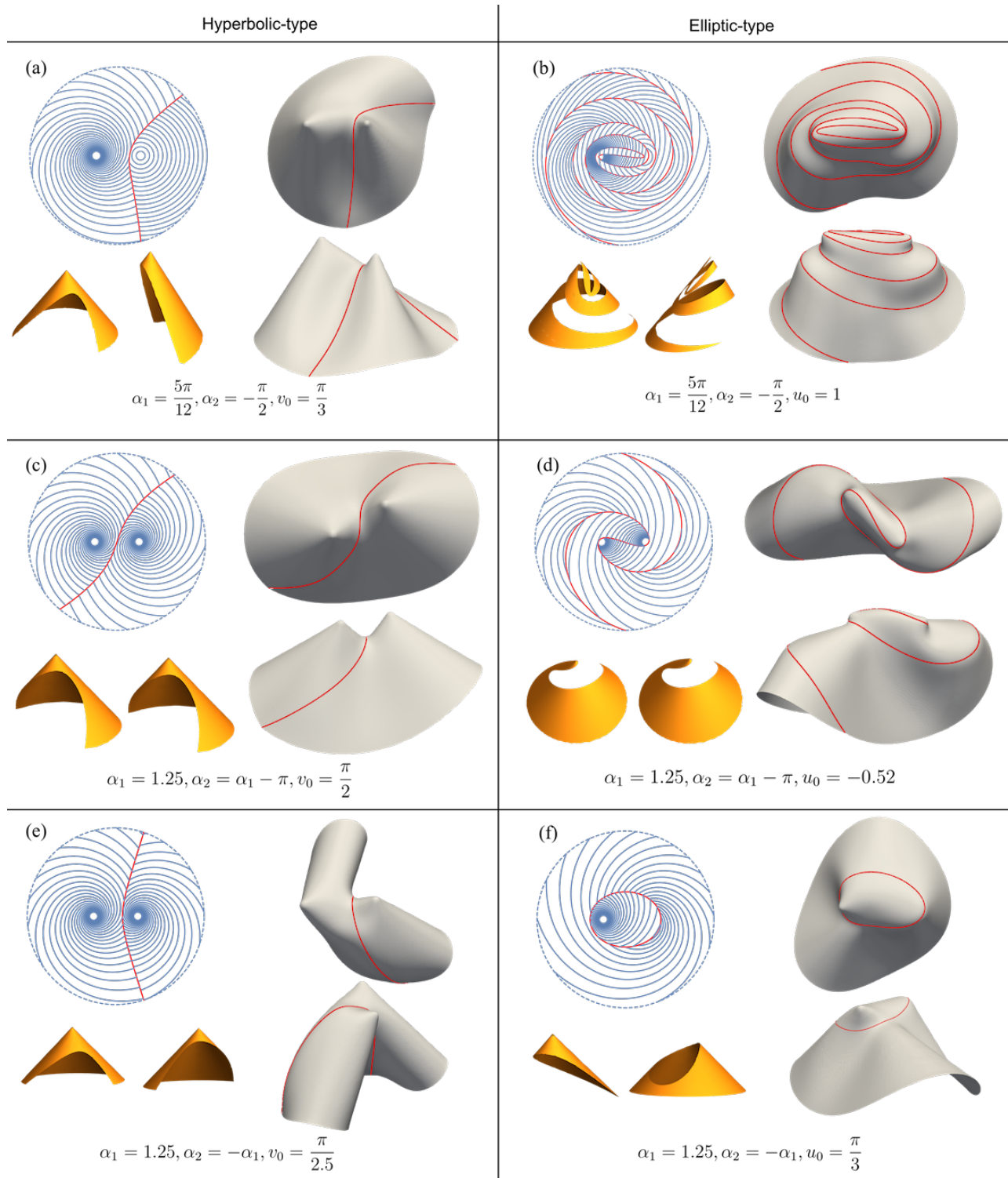


Figure 4: Examples of hyperbolic-type interfaces and their elliptic-type pairs. (a)-(f) Top left: reference domains and their interface. Bottom left: analytical separated cone parts. Top right and bottom right: two views of the simulated configurations obtained by the simulation; image of interface red curve (color on-line). The parameters are provided in the figure panels.

illustrate two examples of the two types of interfaces that have $\alpha_1 = \alpha_2 = \alpha$ (up to $\pm\pi$). Recalling the formulae Eqs. (22) and (25), we have

$$\begin{cases} x(u) = c \cosh u \cos(u \tan \alpha + v_0) \\ y(u) = c \sinh u \sin(u \tan \alpha + v_0) \end{cases} \quad (26)$$

for hyperbolic-type interface passing through $(x(0), y(0)) = (0, 0)$ when $v_0 = \pi/2$, and

$$\begin{cases} x(v) = c \cosh(-v \tan \alpha + u_0) \cos v \\ y(v) = c \sinh(-v \tan \alpha + u_0) \sin v \end{cases} \quad (27)$$

for elliptic-type interface passing through $(x(\pi/2), y(\pi/2)) = (0, 0)$ when $u_0 = \frac{\pi}{2} \tan \alpha$. Examining these two forms, we find that the two interfaces have 180 degree rotation symmetry, as illustrated in Figs. 4(c)(d).

Figs. 4(e)(f) show interfaces between two patterns with equal and opposite spirals, $\alpha_1 = -\alpha_2$ (up to $\pm\pi$ as well), and hence also opposite twists. Notice that for these two cases, the parametric forms of interfaces in Eqs. (22) and (25) degenerate to a hyperbolic interface

$$\begin{cases} x(u) = c \cosh u \cos v_0 \\ y(u) = c \sinh u \sin v_0 \end{cases} \quad (28)$$

and an elliptical interface

$$\begin{cases} x(v) = c \cosh u_0 \cos v \\ y(v) = c \sinh u_0 \sin v \end{cases} \quad (29)$$

Furthermore, the hyperbolic interface degenerates to a straight-line when $v_0 = \pi/2$ as that in Fig. 10(a), which means the interface passes through the origin and bisects the patterns. The separated cone parts generated by conical deformations for each example are provided in Fig. 4, illustrating conical inconsistency. The simulations in Fig. 4 (also in the following figures) show the continuous configurations that achieve local energy minima by blunting the interfaces (red curves) and further isometrically deforming the surfaces outside the non-isometric neighborhood.

Interfaces in circular patterns. Now we briefly discuss the metric-compatible interfaces between two circular patterns. Notice that the analysis for spiral patterns in elliptical coordinates still holds for circular patterns – we only need to replace α_1 and α_2 by $\pm\pi/2$. Without loss of generality, we choose $\alpha_1 = \pi/2$ and $\alpha_2 = -\pi/2$. The other choices of $\pi/2$ or $-\pi/2$ generate no new cases. Then the hyperbolic-type interface (22) and the elliptic-type interface (25) degenerate to a hyperbola and an ellipse respectively, with the same expressions as Eq. (28) and Eq. (29) – hence our nomenclature above of hyperbolic-type and elliptic-type. Fig. 1 illustrates three interfaces between two circular patterns: straight-line, hyperbolic, and elliptical interfaces, determined by the constants v_0 and u_0 in (28) and (29). For more details of the actuated states and complex topographies on combining circular patterns, we refer to previous work [18].

3.2 Continuous-director interfaces

A trivial “interface” between two spiral patterns is the so-called continuous-director interface. That is, the directors \mathbf{n}_1 and \mathbf{n}_2 are parallel across the interface, and a director field integral curve (blue,

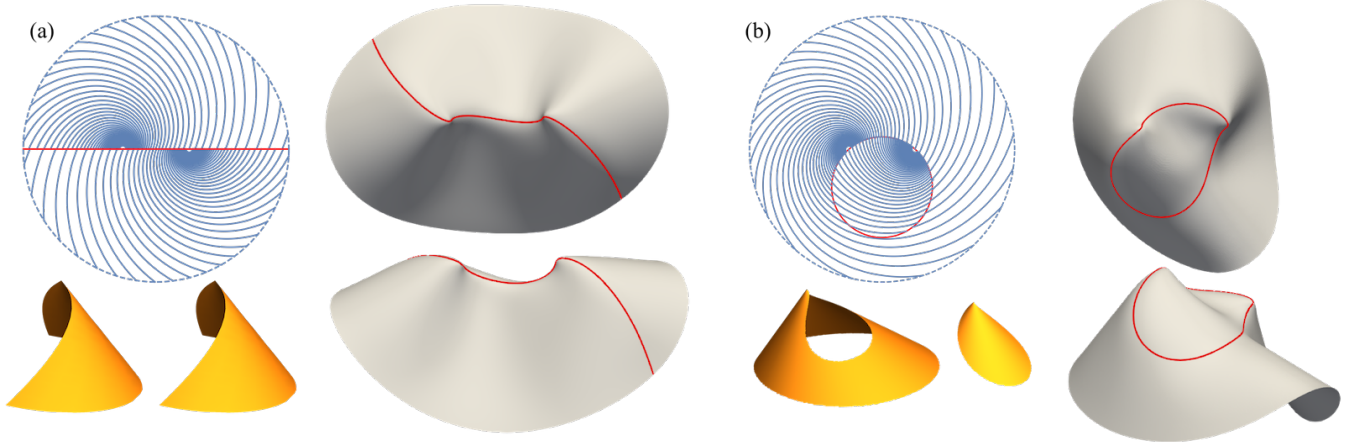


Figure 5: (a)-(b) Top left: reference domains. Bottom left: analytical separated cone parts. Top right and bottom right: two views of the actuated configurations obtained by the simulation. The metric-compatible interface between two smoothly meeting spiral patterns is (a) the horizontal axis for $\alpha_1 = \alpha_2$ (here = 1.173); (b) a circle for $\alpha_1 \neq \alpha_2$ and $\alpha_1 \neq \alpha_2 \pm \pi$ (here $\alpha_1 = 1.173$ and $\alpha_2 = -1.249$).

see Fig. 5a) suffers no kink upon crossing the interface. The metric compatibility condition holds trivially by substituting $\mathbf{n}_1 = \pm \mathbf{n}_2$ into Eq. (15). Establishing the coordinate system in Fig. 3, the directors \mathbf{n}_1 and \mathbf{n}_2 at position $\mathbf{x} = (c \cosh u \cos v, c \sinh u \sin v)$ again have the forms

$$\mathbf{n}_1(\mathbf{x}) = \mathbf{R}(\alpha_1) \frac{\mathbf{x} - \mathbf{c}_1}{|\mathbf{x} - \mathbf{c}_1|}, \quad \mathbf{n}_2(\mathbf{x}) = \mathbf{R}(\alpha_2) \frac{\mathbf{x} - \mathbf{c}_2}{|\mathbf{x} - \mathbf{c}_2|}, \quad (30)$$

where $\mathbf{c}_1 = (-c, 0)$, $\mathbf{c}_2 = (c, 0)$ and $\mathbf{R}(\cdot) = \cos(\cdot)(\mathbf{e}_1 \otimes \mathbf{e}_1 + \mathbf{e}_2 \otimes \mathbf{e}_2) + \sin(\cdot)(-\mathbf{e}_1 \otimes \mathbf{e}_2 + \mathbf{e}_2 \otimes \mathbf{e}_1)$ is a rotation in \mathbb{R}^2 . Recalling $|\mathbf{n}_1(\mathbf{x})| = |\mathbf{n}_2(\mathbf{x})| = 1$, we have

$$\mathbf{n}_1(\mathbf{x}) = \pm \mathbf{n}_2(\mathbf{x}) \Leftrightarrow (\mathbf{n}_1(\mathbf{x}) \cdot \mathbf{e}_1)(\mathbf{n}_2(\mathbf{x}) \cdot \mathbf{e}_2) = (\mathbf{n}_1(\mathbf{x}) \cdot \mathbf{e}_2)(\mathbf{n}_2(\mathbf{x}) \cdot \mathbf{e}_1). \quad (31)$$

The latter condition expresses equal tangents of the angles the directors make with \mathbf{e}_1 and eliminates the modulus denominators of Eq. (30). Substituting expression Eq. (17) for \mathbf{x} and Eq. (30), a direct calculation of Eq. (31) yields

$$\sin(\alpha_1 - \alpha_2)(\sin^2 v - \sinh^2 u) + 2 \cos(\alpha_1 - \alpha_2) \sin v \sinh u = 0. \quad (32)$$

We have the following two cases depending on $(\alpha_1 - \alpha_2)$:

- $\alpha_1 = \alpha_2$ or $\alpha_1 - \alpha_2 = \pm \pi$. Eq. (32) implies $\sin v \sinh u = 0 = y$, then the interface is the horizontal axis, as depicted in Fig. 5(a). We reparameterize the interface by

$$\mathbf{x}(l) = (l, 0), \quad l \in \mathbb{R}. \quad (33)$$

- $\alpha_1 \neq \alpha_2$ and $\alpha_1 - \alpha_2 \neq \pm \pi$. Eq. (32) is equivalent to

$$x^2 + \left(y - \frac{c}{\tan(\alpha_1 - \alpha_2)} \right)^2 = \frac{c^2}{\sin^2(\alpha_1 - \alpha_2)} \quad (34)$$

by substituting $(x, y) = (c \cosh u \cos v, c \sinh u \sin v)$. Clearly, the interface (34) is a circle with radius $c/|\sin(\alpha_1 - \alpha_2)|$ and center $(0, c/\tan(\alpha_1 - \alpha_2))$, as depicted in Fig. 5(b). The circle becomes $x^2 + y^2 = c^2$ when $\alpha_1 - \alpha_2 = \pm\pi/2$. We can parameterize the interface by

$$\mathbf{x}(\theta) = \left(0, \frac{c}{\tan(\alpha_1 - \alpha_2)}\right) + \frac{c}{|\sin(\alpha_1 - \alpha_2)|}(\cos \theta, \sin \theta), \quad \theta \in [0, 2\pi). \quad (35)$$

The degeneracy $\alpha_1 - \alpha_2 = \pm\pi$ of (32) only occurs for circular patterns since the constant α for spiral patterns is not equal to $\pm\pi/2$ and is restricted in $(-\pi/2, -\alpha_c) \cup (\alpha_c, \pi/2)$ for forming cones.

3.3 Interfaces between concentric spirals

We now consider the interfaces between two spiral patterns centered at the same position $(0, 0)$, i.e., $c = 0$. The elliptical coordinates are not appropriate for this situation, so we write the directors $\mathbf{n}_1 = (\cos(\theta + \alpha_1), \sin(\theta + \alpha_1))$ and $\mathbf{n}_2 = (\cos(\theta + \alpha_2), \sin(\theta + \alpha_2))$ at the position (r, θ) in polar coordinates. Assuming $\alpha_1 \neq \alpha_2$ (the case $\alpha_1 = \alpha_2$ is trivial), the tangent \mathbf{t} has two solutions

$$\mathbf{t} = \pm \frac{\mathbf{n}_1 + \mathbf{n}_2}{|\mathbf{n}_1 + \mathbf{n}_2|} \Leftrightarrow \mathbf{t} = \pm \left(\cos \left(\frac{\alpha_1 + \alpha_2}{2} + \theta \right), \sin \left(\frac{\alpha_1 + \alpha_2}{2} + \theta \right) \right) \quad (36)$$

and

$$\mathbf{t} = \pm \frac{\mathbf{n}_1 - \mathbf{n}_2}{|\mathbf{n}_1 - \mathbf{n}_2|} \Leftrightarrow \mathbf{t} = \pm \left(\cos \left(\frac{\alpha_1 + \alpha_2 + \pi}{2} + \theta \right), \sin \left(\frac{\alpha_1 + \alpha_2 + \pi}{2} + \theta \right) \right) \quad (37)$$

which correspond to the two spirals with parameters $\alpha = \bar{\alpha} = (\alpha_1 + \alpha_2)/2$ and $\alpha = (\alpha_1 + \alpha_2)/2 + \pi/2$ respectively, when $\alpha_1 + \alpha_2 \neq 0, \pm\pi$, and where $\bar{\alpha} = (\alpha_1 + \alpha_2)/2$ is the average spiral parameter, which defines a curve that the two directors meet at equal angles. Specifically, the interface is a logarithmic spiral of the form

$$r(\theta) = r_0 \exp \left(\frac{\theta}{\tan \bar{\alpha}} \right), \quad (38)$$

corresponding to the interface in Fig. 6(a), or the form

$$r(\theta) = r_0 \exp \left(\frac{\theta}{\tan(\bar{\alpha} + \pi/2)} \right) \quad (39)$$

corresponding to the interface in Fig. 6(b). Here we construct two interfaces in each of Figs. 6(a)(b), so that the domain is divided into two subdomains occupied by the two spiral patterns (one is a circular pattern for the particular example) respectively.

The idea can be simply generalized to n concentric spiral patterns with the spiral constants α_i , $i = 1, 2, \dots, n$. Then the interface between the i -th pattern and the $(i+1)$ -th pattern is a logarithmic spiral with the spiral constant $(\alpha_i + \alpha_{i+1})/2$ or $(\alpha_i + \alpha_{i+1})/2 + \pi/2$, for $i = 1, 2, \dots, n$ and we define $\alpha_{n+1} = \alpha_1$. However, interfacial spirals will generically intersect, dividing the domain into regions that would actuate into facets in the target space. However, we see relaxation of boundaries in the simulations of Fig. 6(a), and so these facets would presumably also relax.

For the cases $\alpha_1 + \alpha_2 = 0, \pm\pi$, the interface degenerates to a radial line [Fig. 6(c)] parameterized as

$$\mathbf{x}(r) = (r \cos \xi, r \sin \xi), \quad r \in [0, R], \quad (40)$$

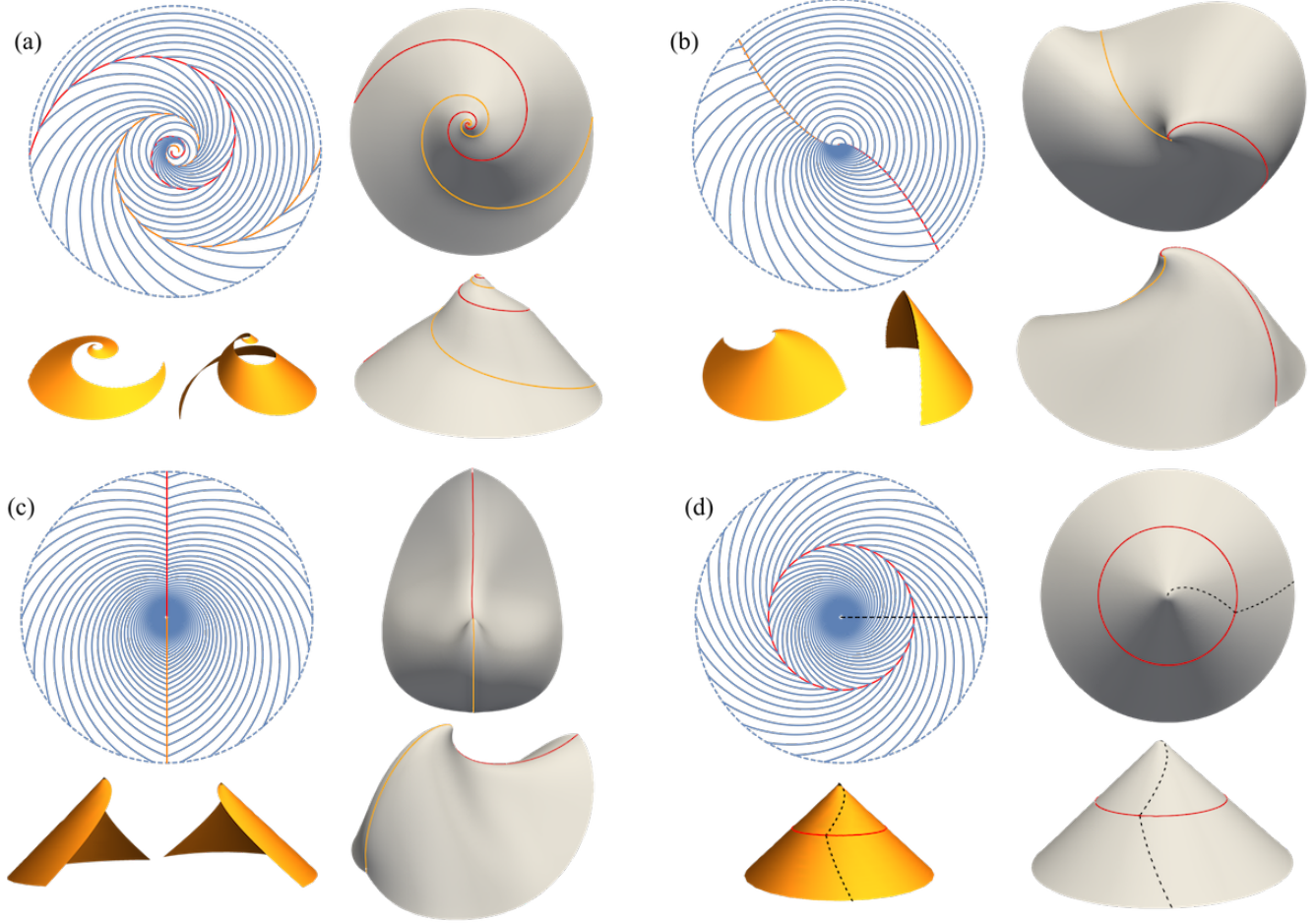


Figure 6: (a)-(d) Examples of concentric spiral interfaces. Top left: reference domains. Bottom left: analytical separated cone parts. Top right and bottom right: actuated configurations obtained by the simulation. (a)-(b) The concentric spiral interface between a spiral pattern with $\alpha_1 = 1$ and a circular pattern with $\alpha_2 = \pi/2$. The spiral interface has the spiral parameter (a) $\alpha = (\alpha_1 + \alpha_2)/2$ and (b) $\alpha = (\alpha_1 + \alpha_2)/2 + \pi/2$. The orange spiral interface is constructed by rotating the red one by π . (c)-(d) The radial line interface (c) and the circular interface (d) between two spiral patterns with $\alpha_1 = 1.2$ and $\alpha_2 = -1.2$. The actuated state with the circular interface is geometrically consistent under the cone deformations, with the two domains having the opposite relative rotations indicated by the radial dashed line in black before and after actuation.

where $\xi \in [0, 2\pi)$ is a constant angle denoting the radial direction and R is the radius of the reference domain, or degenerates to a circle with the same center [Fig. 6(d)] parameterized as

$$\mathbf{x}(\theta) = (\bar{r} \cos \theta, \bar{r} \sin \theta), \quad \theta \in [0, 2\pi), \quad (41)$$

where $0 < \bar{r} < R$ is the radius of the interface. As illustrated in Fig. 6(d), the actuated state is a cone, which is conically consistent. The two domains have the opposite rotations relative to the interface upon actuation, indicated by the actuated radial dashed line in black.

Summary. By considering the situations $c = 0$ or $c \neq 0$, $\mathbf{n}_1 = \pm \mathbf{n}_2$ or $\mathbf{n}_1 \neq \pm \mathbf{n}_2$, we have

characterized all possible metric-compatible interfaces between two spiral patterns: hyperbolic-type, elliptic-type, concentric spiral and continuous-director interfaces. We term the interface with $\mathbf{n}_1 \neq \pm \mathbf{n}_2$ the *twinning case*, and the interface with $\mathbf{n}_1 = \pm \mathbf{n}_2$ the *continuous-director case*. Namely, the hyperbolic-type, elliptic-type and concentric interfaces belong to the twinning case, and the two continuous-director interfaces in Fig. 5 belong to the continuous-director case.

3.4 Interfaces in anticones, cone-complements, orthogonal duals, and complex patterns

In the previous discussion, we have systematically found all possible metric-compatible interfaces between two spiral patterns, by solving the metric compatibility condition (15). We assume that: 1. The two patterns evolve into cones so that we can use the explicit cone deformations (13) to study the deformed interfaces; 2. The director \mathbf{n}_1 (\mathbf{n}_2) on the left (right) side of the interface is associated with the left (right) pattern when $c \neq 0$. In this subsection, we generalize the method of constructing patterns in several natural ways, extending it to more complex intersections of circles and spirals, and thereby show that the class of metric-compatible interfaces is even richer.

First of all, the method is also applicable to spiral/radial patterns that evolve into anticones. Fig. 7(b) illustrates a hyperbolic-type interface between a spiral pattern with $\alpha_1 = 5\pi/12$ and a radial pattern with $\alpha_2 = 0$. The spiral pattern evolves into a cone with positive GC localized at the tip, whereas the radial pattern evolves into an anticone with negative GC localized at the tip. The simulation in Fig. 7(b) illustrates the feature of the combination of cone-like and anticone-like structures.

Next, we can construct new metric-compatible patterns by taking the *complements* of the existing ones. For example, the complement of the original pattern in Fig. 7(a) is the pattern in Fig. 7(c) constructed by combining the initially hidden parts of spiral/circular patterns on the other side of the interface with each other. The original pattern satisfies the metric compatibility condition (15), i.e., $|\mathbf{n}_1 \cdot \mathbf{t}| = |\mathbf{n}_2 \cdot \mathbf{t}|$. This implies that the complement pattern is also metric-compatible at the same interface, because the director of the complement at the interface becomes \mathbf{n}_2 on the left side and \mathbf{n}_1 on the right side, then the condition $\mathbf{n}_1 \cdot \mathbf{t} = \mathbf{n}_2 \cdot \mathbf{t}$ still holds. This construction relies on the smoothness of each pattern across the interface. It is worthwhile mentioning that the virtual centers of the spiral pattern and the circular pattern in the complement are located at the same places as those real centers were in the original pattern. In the original pattern, these centers deform into the tips of cones, which are point defects of Gaussian curvature. These point defects are found to play a crucial role in the mechanical behaviour of thin sheets [47, 51, 56]. By removing the centers, we anticipate complements will have significantly different mechanical properties, as illustrated by the comparison between the simulations in Fig. 7(a) and (c), the latter having no tips.

Furthermore, another way of constructing a different metric-compatible pattern is taking the *orthogonal dual* of the original one. The orthogonal dual of the original pattern with director field $\mathbf{n}(\mathbf{x})$ is the pattern with director field $\mathbf{n}^\perp(\mathbf{x})$, where $\mathbf{n}^\perp(\mathbf{x}) = \mathbf{R}(\pi/2)\mathbf{n}(\mathbf{x})$ is perpendicular to $\mathbf{n}(\mathbf{x})$. For example, the orthogonal dual of a circular pattern is the radial pattern with director pointing along the radial direction. Upon actuation, the orthogonal dual deforms to an anticone, whereas the circular pattern deforms to a cone [30, 15]. A metric-compatible interface between two patterns is still metric-compatible after taking the orthogonal duals by the fact that

$$|\mathbf{n}_1 \cdot \mathbf{t}| = |\mathbf{n}_2 \cdot \mathbf{t}| \Leftrightarrow |\mathbf{n}_1^\perp \cdot \mathbf{t}| = |\mathbf{n}_2^\perp \cdot \mathbf{t}|. \quad (42)$$

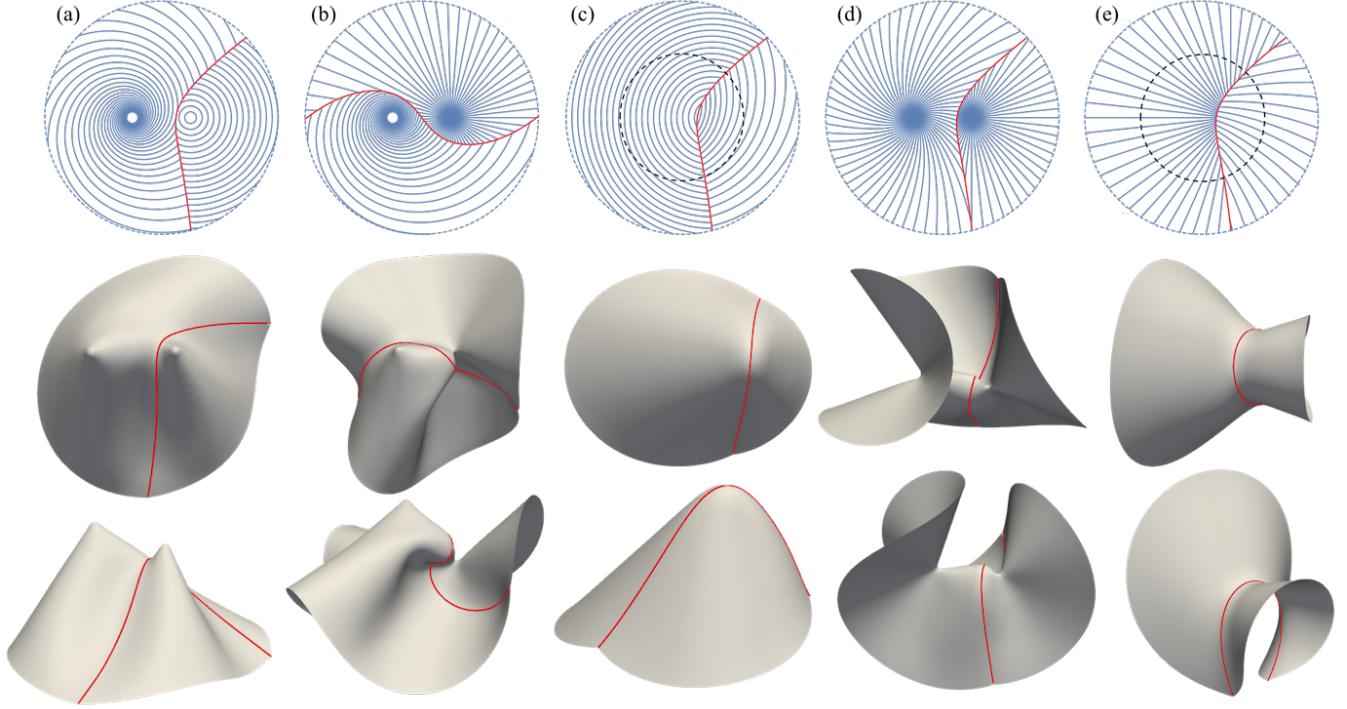


Figure 7: Top row: reference domains. Middle and bottom rows: two views of the actuated configurations obtained by the simulation. (a) The hyperbolic-type interface between a spiral pattern with $\alpha_1 = 5\pi/12$ and a circular pattern with $\alpha_2 = -\pi/2$. (b) The hyperbolic-type interface between a spiral pattern with $\alpha_1 = 5\pi/12$ and a radial pattern with $\alpha_2 = 0$. (c) The complement of the pattern in (a). (d) The orthogonal dual of the pattern in (a). (e) The complement of the orthogonal dual. The reference domains of the simulations for (c) and (e) are the smaller circular domains within the dashed circles for the sake of clarity.

Fig. 7(d) shows the orthogonal dual of the original pattern in Fig. 7(a), with its complement in Fig. 7(e).

We end up the interface section with a discussion about the prospect of designing complex patterns by combining spiral patterns as building blocks. A previous work [18] shows that symmetric and irregular patterns can be designed with circular patterns as building blocks, and the complex topographies actuated from the patterns can further be inverse designed. In spiral patterns, the straight-line interface between two equal and opposite spirals is a promising candidate to design symmetric patterns. Fig. 8(a) shows an example of 2×2 symmetric pattern, which can be extended to an infinitely large pattern by translating the domain systematically. The large pattern is generically multistable – the tips of the actuated cones can deform up or down, depending on the initial direction of perturbation. For example, the simulations in Fig. 8(a) show two stable states: the left simulation has all the four tips popping up whereas the right simulation has one tip popping down. Breaking the symmetry, one can design an irregular pattern consisting of different spiral/circular patterns separated by different types of metric-compatible interfaces, e.g. Fig. 8(b). However, the design of a large pattern is expected to be difficult – the shapes of the interfaces are highly irregular and hence the intersections are hard to predict. An example of the mixture

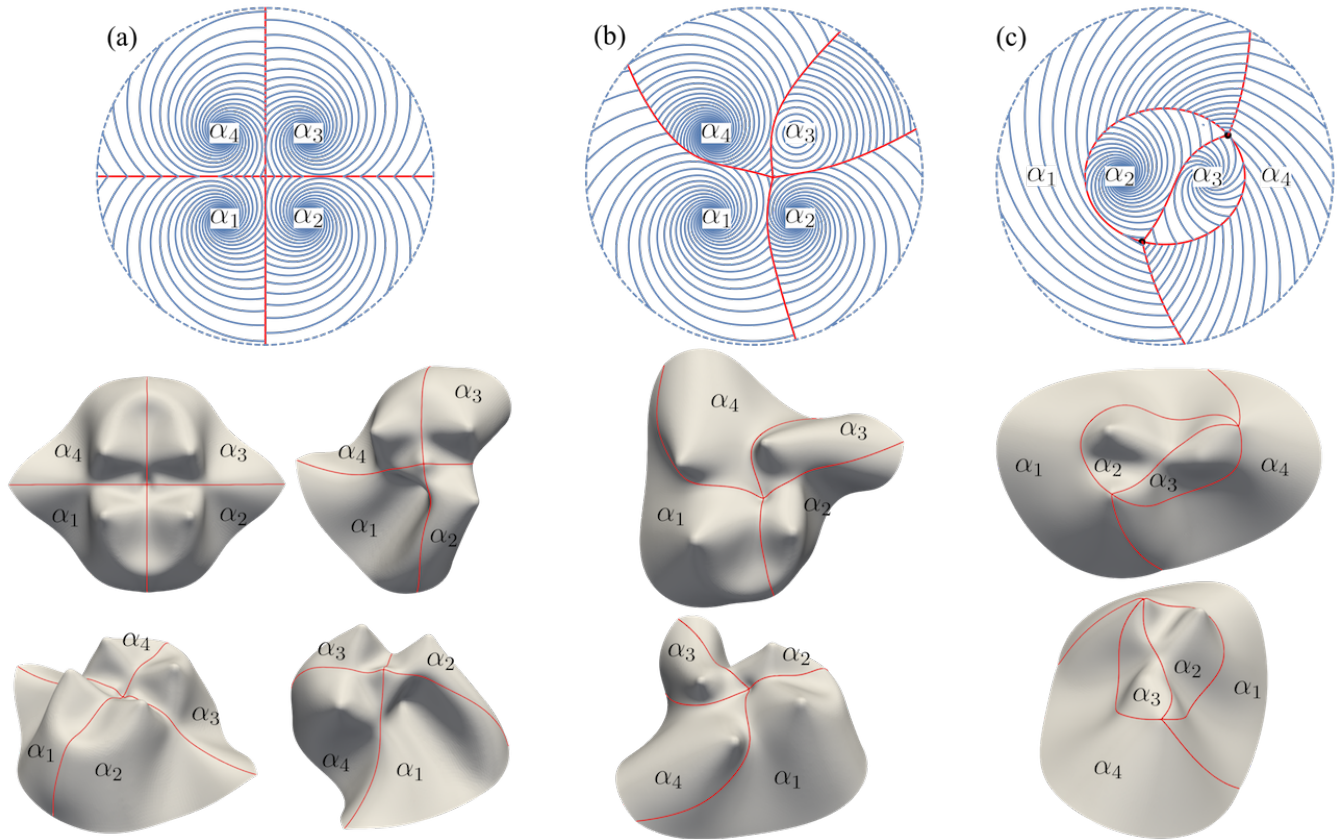


Figure 8: Examples of the complex patterns. Two views (middle row and bottom row) are provided for each simulated configuration. (a) A 2×2 symmetric array of spiral patterns with $(\alpha_1, \alpha_2, \alpha_3, \alpha_4) = (1.25, -1.25, 1.25, -1.25)$ separated by straight-line interfaces. Two simulations are provided to illustrate the multistability: All the four tips can pop up (left simulation) or one of the tips can pop down (right simulation). (b) An irregular 2×2 array of spiral/circular patterns with $(\alpha_1, \alpha_2, \alpha_3, \alpha_4) = (1.25, -1.25, \pi/2, 5\pi/12)$. (c) A mixture of elliptic and hyperbolic-type interfaces with $(\alpha_1, \alpha_2, \alpha_3, \alpha_4) = (-1.25, 1.25, 1, -1)$.

of hyperbolic-type and elliptic-type interfaces is given in Fig. 8(c). The topographies evolved from these large spiral patterns are also expected to be more complex because of conical inconsistency. However, one recurring theme is that intersections of boundaries typically generate a point-like angular deficit, and hence a tip in the actuated surface.

4 Geometric requirements for further isometries

Despite obeying the local metric change induced by the director, the deformation that maps a general director pattern to its actuated state is not unique. Consequently, the resultant deformed interface between two patterns is not unique. This is because the metric change only determines the first fundamental form of a surface, whereas the second fundamental form is still unknown. For spiral and circular patterns, the simplest deformations satisfying the metric change are the cone deformations

(13) and (14). In [18], it is proved that the shapes of the actuated, metric-compatible interfaces obtaining under the cone deformations between circular patterns are the same – the interfaces are conically consistent, since the two pieces of cone can be fitted together without further isometries from conical to make them match. To be specific, let $\mathbf{x}(u)$ denote the metric-compatible interface and $\mathbf{c}_1, \mathbf{c}_2$ be the centers of two circular patterns. Then, there exists a constant rotation $\mathbf{R} \in SO(3)$ and a constant translation $\mathbf{h} \in \mathbb{R}^3$ such that $\mathbf{R}\mathbf{y}_c(\mathbf{x}(u) - \mathbf{c}_1) + \mathbf{h} = \mathbf{y}_c(\mathbf{x}(u) - \mathbf{c}_2)$, where \mathbf{y}_c is the cone deformation for circular patterns defined by Eq. (14).

However, generically, the deformed metric-compatible interfaces \mathbf{y}_{α_1} and \mathbf{y}_{α_2} between spiral patterns are not geometrically consistent under their cone deformations, unless the spiral constants are $|\alpha_1| = |\alpha_2| = \pi/2$, i.e., the two spiral patterns degenerate to circular patterns. These phenomena can be seen in the examples of conically consistent interfaces in circular patterns [Fig. 1] and geometrically inconsistent interfaces in spiral patterns [Figs. 4, 5 and 6]. The problem is that deformations of spirals carry rotations, see after Eq. (8) and after Eq. (13), and that these rotations, stemming from each side of the metric-compatible line, rotate its elements differently on actuation into a crease. An example is in Fig. 4(a) where the boundary evolved under the circular pattern suffers no rotations, whereas that under the spiral suffers rotations dependent upon the distance from the spiral center to the metric-compatible line in the reference state. Explicitly, suppose a hyperbolic-type metric-compatible interface is $\mathbf{x}(u) = (x(u), y(u))$, calculated from Eq. (22) (and equivalently an elliptic-type metric-compatible interface $\mathbf{x}(v) = (x(v), y(v))$, calculated from Eq. (25)). The centers of the two patterns are $\mathbf{c}_1 = (-c, 0)$ and $\mathbf{c}_2 = (c, 0)$ with $c > 0$. Recalling the cone deformation $\mathbf{y}_\alpha(\mathbf{r})$ in Eqs. (13) and (14), the deformed interfaces $\mathbf{y}_1(u)$ and $\mathbf{y}_2(u)$ mapped by the two cone deformations from two sides yield

$$\begin{aligned}\mathbf{y}_1(u) &= \mathbf{y}_{\alpha_1}(\mathbf{x}(u) - \mathbf{c}_1), \\ \mathbf{y}_2(u) &= \mathbf{y}_{\alpha_2}(\mathbf{x}(u) - \mathbf{c}_2).\end{aligned}\tag{43}$$

For the particular example in Fig. 4(a), we have the parameters $\alpha_1 = 5\pi/12$ and $\alpha_2 = -\pi/2$. We replace $\mathbf{y}_{-\pi/2}(\mathbf{r})$ by the cone deformation $\mathbf{y}_c(\mathbf{r})$ for circular patterns. The cone deformations' rotation angles $-b_{1,2} \ln(r_{1,2}(u)/r_{1,2}(0))$ (recall Eq. (13), with $\alpha \neq \pm\pi/2$) in $\mathbf{y}_{1,2}(\mathbf{r})$ are functions of $r_{1,2}(u)$, which generically ($r_1(u) \neq r_2(u)$) leads to different rotations along the interface driven from two sides. As a result, the shapes of the deformed interfaces $\mathbf{y}_1(u)$ and $\mathbf{y}_2(u)$ are generically different. Since bend energy scales as $\sim h^3$ and stretch energy scales as $\sim h$, with h the thickness of the reference LCE sheet, the actuated configuration tends to follow the metric condition as $h \rightarrow 0$, that is, avoiding stretch from the actuated shape. Under this circumstance, it is physically favorable to have two further isometric deformations \mathbf{g}_1 and \mathbf{g}_2 mapping the two interfaces to an identical one $\mathbf{g}(u)$, i.e.,

$$\mathbf{g}(u) := \mathbf{g}_1(\mathbf{y}_1(u)) = \mathbf{g}_2(\mathbf{y}_2(u)).\tag{44}$$

The additional isometries \mathbf{g}_1 and \mathbf{g}_2 preserve the geodesic curvatures of $\mathbf{y}_1(u)$ and $\mathbf{y}_2(u)$, and therefore preserve the concentrated GC discussed in the next section.

5 Gaussian curvature concentrated along a crease

Since geodesic curvature and GC are intrinsic quantities preserved by isometric deformations, we can analytically calculate the distributed GC along the deformed interface resulting from the cone

deformations without considering the additional isometries. We then compare our analytical GC with that of simulations, and see numerically that the simulation yields a configuration satisfying the metric change induced by the director. In other words, the isometries \mathbf{g}_1 and \mathbf{g}_2 that match the interfaces together exist.

We employ three distinct approaches for analytically calculating the GC concentrated along the deformed interface. The first two approaches are based on the typical differential geometry method dealing with the geodesic curvature on the actuated states (cone surface) or the unrolled 2D flat state. The third approach considers the metric change directly from the reference director fields and then applies *Liouville's formula* [38, 15] to calculate the geodesic curvature and the GC. The three approaches are illustrated by the sketch for circular patterns in Fig. 9, but the ideas apply to the general spiral patterns.

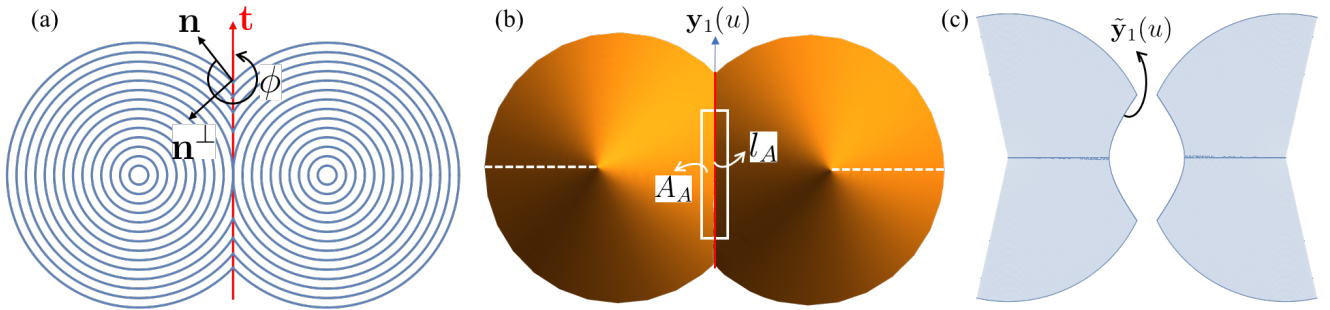


Figure 9: (a) Straight-line interface (red) between two circular patterns. The unit tangent \mathbf{t} of the interface is expressed as $\mathbf{t} = \cos \phi \mathbf{n} + \sin \phi \mathbf{n}^\perp$, where \mathbf{n} is the director and $\mathbf{n} \cdot \mathbf{n}^\perp = 0$. (b) $\mathbf{y}_1(u)$ is the actuated interface deformed from the left circular pattern. The white loop is the Gauss-Bonnet loop composed of two paths along the interface connected by infinitesimal geodesic caps that traverse the interface orthogonally. l_A is the arc length of the actuated interface and A_A is the area enclosed within the loop. The dashed lines are where the cuts are performed to unroll the cones onto the 2D plane in (c). (c) The unrolled states of two separated domains. $\tilde{\mathbf{y}}_1(u)$ is the interface of the left domain after the unrolling process.

5.1 Concentrated GC calculated from the actuated cone

The concentrated GC along the deformed interface is the sum of the two (signed) geodesic curvatures from two sides of an enclosing contour: This argument is consistent with considering the Gauss-Bonnet theorem along a loop containing the interface with the width of the loop tending to zero. By choosing the appropriate Gauss-Bonnet loop, such as that in Fig. 9(b), the Gauss-Bonnet theorem for the actuated domain M within the loop is

$$\int_M K_A dA_A + \oint_{\partial M} \kappa_g ds_A + \sum \beta_i = 2\pi\chi(M), \quad (45)$$

where κ_g is the geodesic curvature along the loop ∂M , the β_i are the discrete turning angles (here at the corners of the loop), ds_A is differential length along the loop, and $\chi(M)$ is the Euler characteristic

of M . Taking the limit of the width of the loop to zero, the Gauss-Bonnet theorem for the actuated interface yields the integrated GC

$$\Omega = \int K_A dA_A = \int (k_{g_1} - k_{g_2}) dl_A \quad (46)$$

after canceling the Euler characteristic term and the turning angle term (both are 2π), and neglecting the geodesic integral along the infinitesimal sections of the contour transverse to the interface. Here Ω is the integrated GC, K_A is the distributed GC within the loop, k_{g_1} and k_{g_2} are the geodesic curvatures of the actuated interfaces $\mathbf{y}_1(u)$ and $\mathbf{y}_2(u)$ from the left side and the right side, A_A is the area within the Gauss-Bonnet loop, and l_A is the arc length along the actuated interface. The actuated arc length l_A can be defined by

$$l_A(u) = \begin{cases} \int_0^u |\mathbf{y}'_1(u)| du, & \text{if } u \geq 0 \\ -\int_u^0 |\mathbf{y}'_1(u)| du, & \text{if } u < 0 \end{cases} \quad (47)$$

in which we define $l_A(0) = 0$ as the reference point. Since $l_A(u)$ is monotonically increasing, we can find its inverse as $u = \bar{u}(l_A)$. The arc length l_A derived from $\mathbf{y}_1(u)$ is consistent with that from $\mathbf{y}_2(u)$ by the metric-compatibility condition $|\mathbf{y}'_1(u)| = |\mathbf{y}'_2(u)|$. This equivalence allowed us to transform $\oint_{\partial M} \kappa_g ds_A$ of (45), a loop integral, to $\int (k_{g_1} - k_{g_2}) dl_A$ of (46), a line integral along the crease. (The sign in $-k_{g_2}$ reflecting the different direction in that side of the loop integral compared with along dl_A . We then define $d\Omega/dl_A$ as the concentrated GC per unit actuated arc length.

However, it is usually convenient to write the geometrical quantities in terms of the parametric parameter u of the reference space metric-compatible interface. Consequently, the integrated GC, Ω , in terms of u is

$$\Omega = \int K_A dA_A = \int (k_{g_1} - k_{g_2}) \frac{dl_A}{du} du, \quad (48)$$

where $\frac{dl_A}{du} = |\mathbf{y}'_1(u)| = |\mathbf{y}'_2(u)|$ is the Jacobian. The κ_{g_i} can be calculated, by standard methods of differential geometry, in terms of derivatives of $\mathbf{y}_i(u)$ with respect to u and in terms of the local normal vector to the cone i . Then the concentrated GC in terms of the parametric reference state parameter u is

$$\frac{d\Omega}{du} = (\kappa_{g_1}(u) - \kappa_{g_2}(u)) \frac{dl_A}{du}, \quad (49)$$

and accordingly the concentrated GC per unit actuated arc length along the seam is

$$\frac{d\Omega}{dl_A} = \kappa_{g_1}(\bar{u}(l_A)) - \kappa_{g_2}(\bar{u}(l_A)). \quad (50)$$

5.2 Concentrated GC calculated by unrolling the actuated cone

A cone has a center of concentrated Gaussian curvature, i.e. the cone surface is Gaussian flat everywhere except for the tip. We can then cut a cone along its slant flank and unroll it onto the 2D plane isometrically with the angular deficit $2\pi(1 - \sin \varphi)$, where φ is the cone angle. Accordingly, the actuated interface is then mapped to a curve on the 2D plane. As an example, we perform the unrolling process separately for the two actuated cones in Fig. 9(b) yielding the unrolled configurations in Fig. 9(c) with their interface boundaries. This procedure will simplify the calculation of

geodesic curvature – one can calculate the total curvature of the 2D curve instead to obtain the equivalent geodesic curvature. The approach essentially uses the basic differential geometric idea that the geodesic curvature is preserved by isometric deformations (here the unrolling process).

Let (x, y, z) denote a point on the cone surface, which is parameterized by (r, θ) with the form

$$x = r \sin \varphi \cos \theta, \quad y = r \sin \varphi \sin \theta, \quad z = -r \cos \varphi, \quad (51)$$

where $\theta \in [-\pi, \pi]$ and φ is the cone angle. The cone surface is obtained by applying the cone deformation \mathbf{y}_{α_i} on the reference domain \mathcal{D}_i . The deformed interface, as described above, has the parametric form $\mathbf{y}_i(u)$. The cut-and-unroll process takes the angle θ in Eq. (51) to $\theta \sin \varphi$ by considering the angular deficit induced by the unrolling with the cone angle φ . Then the point (x, y, z) parameterized by (r, θ) in Eq. (51) is mapped to $(r \cos(\theta \sin \varphi), r \sin(\theta \sin \varphi))$ in 2D. Specifically, for the actuated interface $\mathbf{y}_1(u)$ in Eq. (43), the unrolled 2D curve is then

$$\begin{cases} \tilde{x}(u) = |\mathbf{y}_1(u)| \cos[\theta(u) \sin \varphi_1] \\ \tilde{y}(u) = |\mathbf{y}_1(u)| \sin[\theta(u) \sin \varphi_1] \end{cases} \quad (52)$$

by substituting $(x, y, z) = \mathbf{y}_1(u)$, where $\theta(u) = \text{sign}(\mathbf{y}_1(u) \cdot \mathbf{e}_2) \arccos \left[\frac{\mathbf{y}_1(u) \cdot \mathbf{e}_1}{|\mathbf{y}_1(u)| \sin \varphi_1} \right] \in [-\pi, \pi]$ is the angle between the point on $\mathbf{y}_1(u)$ and \mathbf{e}_1 after projecting onto $\{\mathbf{e}_1, \mathbf{e}_2\}$ plane. The unrolled interface $\tilde{\mathbf{y}}_1(u)$ is then given by $\tilde{\mathbf{y}}_1(u) = (\tilde{x}(u), \tilde{y}(u))$. This unrolling process is isometric and thus preserves the geodesic curvature. Following the standard method in differential geometry, the geodesic curvature κ_{g_1} of the curve $(\tilde{x}(u), \tilde{y}(u))$ on the 2D plane is the same as the total curvature, i.e.,

$$\kappa_{g_1}(u) = \frac{\tilde{x}'\tilde{y}'' - \tilde{y}'\tilde{x}''}{(\tilde{x}'^2 + \tilde{y}'^2)^{3/2}}. \quad (53)$$

Then we can apply the same approach to reparameterize $\kappa_{g_1}(u)$ in terms of l_A , the arc length of the actuated interface. The same approach applies to calculating $\kappa_{g_2}(u)$, and then the calculation of the concentrated GC follows via (49).

5.3 Concentrated GC calculated from the reference director fields

GC is an intrinsic geometrical quantity that can be derived from the metric change induced by actuation determined by a (reference state) director distribution. Thus the director pattern determines the GC distribution over the entire actuated configuration, including point and curve defects [15]. A useful method for deriving the geodesic curvature of curve defects after actuation is to use Liouville's formula [38]. Specifically, given an orthonormal coordinate system², (u, v) , with the metric tensor $\text{diag}(E, G)$, the geodesic curvature of a reference state, arc-length parameterized curve $(u(l), v(l))$ is

$$\kappa_g = \phi' - \frac{1}{2\sqrt{EG}}(u'E_v - v'G_u), \quad (54)$$

where ϕ is the angle between the tangent \mathbf{t} of the curve and the u -line.

²We use the standard notation (u, v) in differential geometry as the basis. It should be distinguished from the elliptical coordinates in Sect. 3.1.

Here we employ Liouville's formula to derive the geodesic curvature and the Gaussian curvature concentrated along the metric-compatible interfaces for both the twinning cases (hyperbolic-type, elliptic-type and concentric spiral interfaces) and the continuous-director cases. Suppose the arc length parameterized curve $\mathbf{r}(l) = (x(l), y(l))$ is defined on the reference domain of a director pattern. The unit tangent \mathbf{t} of $\mathbf{r}(l)$ is simply $\mathbf{t} = \mathbf{r}'(l)$. It is natural to take the director \mathbf{n} and its perpendicular vector \mathbf{n}^\perp as the u and v basis respectively and then ϕ is the angle rotating \mathbf{n} to \mathbf{t} counterclockwise (see Fig. 9(a)). Following Liouville's formula (54) and the metric tensor (see [37]) associated with $\mathbf{r}(l)$, the geodesic curvature of $\mathbf{r}(l)$ after actuation, derived in [15], is

$$\kappa_g = \frac{\lambda^{1-\nu}}{(\lambda^2 \cos^2 \phi + \lambda^{-2\nu} \sin^2 \phi)^{3/2}} \frac{d\phi}{dl} + \frac{\lambda^{-1-\nu} s \sin \phi + \lambda^{1+\nu} b \cos \phi}{\sqrt{\lambda^2 \cos^2 \phi + \lambda^{-2\nu} \sin^2 \phi}}, \quad (55)$$

where ϕ , obtained by $\mathbf{t} = \cos \phi \mathbf{n} + \sin \phi \mathbf{n}^\perp$, is the angle between the curve tangent \mathbf{t} and the director \mathbf{n} , while b and s are the 2D *bend* and *splay* [37] defined by

$$b = \nabla \times \mathbf{n} = \mathbf{n} \cdot \nabla \psi, \quad s = \nabla \cdot \mathbf{n} = \mathbf{n}^\perp \cdot \nabla \psi, \quad (56)$$

recalling $\mathbf{n} = \cos \psi \mathbf{e}_1 + \sin \psi \mathbf{e}_2$. For the spiral pattern, we have $\psi = \theta + \alpha$ (Eq. (2)). Applying the gradient tensor in polar coordinates, we have

$$b = \sin \alpha / r, \quad s = \cos \alpha / r, \quad (57)$$

where r is the distance between the spiral center and the point we consider.

We employ the formula (55) for geodesic curvature to obtain the concentrated GC along the actuated interface. Notice that the metric tensor $\mathbf{a} = \mathbf{U}_\mathbf{n}^T \mathbf{U}_\mathbf{n}$ is invariant under the transformation $\mathbf{n} \rightarrow -\mathbf{n}$. Thus the resulting metric change and the induced geodesic curvature (55) are also invariant. This can be seen by rewriting Eq. (55) equivalently in terms of the bend, splay, tangent vectors and the metric tensor:

$$\kappa_g = \frac{\lambda^{1-\nu}}{(\mathbf{t} \cdot \mathbf{a} \cdot \mathbf{t})^{3/2}} \frac{d\phi}{dl} + \frac{\lambda^{1+\nu} \mathbf{b} \cdot \mathbf{t}^\perp - \lambda^{-(1+\nu)} \mathbf{s} \cdot \mathbf{t}^\perp}{\sqrt{\mathbf{t} \cdot \mathbf{a} \cdot \mathbf{t}}}, \quad (58)$$

where $\mathbf{t}^\perp = \mathbf{R}(\pi/2)\mathbf{t}$ is the unit vector perpendicular to \mathbf{t} . We define the bend vector \mathbf{b} and the splay vector \mathbf{s} in Eq. (58) as

$$\mathbf{b} = b\mathbf{n}^\perp, \quad \mathbf{s} = s\mathbf{n}, \quad (59)$$

which are invariant under $\mathbf{n} \rightarrow -\mathbf{n}$ since the transformation induces a minus sign in b , s , \mathbf{n} and \mathbf{n}^\perp . Following Eq. (48), the integrated GC is of the form

$$(\textit{Twinning case:}) \quad \Omega = \int K_A dA = \int \left(\frac{2\lambda^{1-\nu}}{\mathbf{t} \cdot \mathbf{a} \cdot \mathbf{t}} \phi'(l) + (\lambda^{1+\nu} \Delta \mathbf{b}^\perp - \lambda^{-(1+\nu)} \Delta \mathbf{s}^\perp) \right) dl, \quad (60)$$

when the directors on the two sides of the interface are not parallel, i.e., $\mathbf{n}_1 \neq \pm \mathbf{n}_2$. Here we have used the facts that $\phi'(l) = \frac{d\phi_1}{dl} = -\frac{d\phi_2}{dl}$ and $dl_A/dl = \sqrt{\mathbf{t} \cdot \mathbf{a} \cdot \mathbf{t}} = \sqrt{\mathbf{t} \cdot \mathbf{a}_1 \cdot \mathbf{t}} = \sqrt{\mathbf{t} \cdot \mathbf{a}_2 \cdot \mathbf{t}}$ given by metric compatibility when $\mathbf{n}_1 \neq \pm \mathbf{n}_2$. In Eq. (60), we also define the perpendicular jumps of the bend and splay vectors as

$$\Delta \mathbf{b}^\perp = (\mathbf{b}_1 - \mathbf{b}_2) \cdot \mathbf{t}^\perp \quad \text{and} \quad \Delta \mathbf{s}^\perp = (\mathbf{s}_1 - \mathbf{s}_2) \cdot \mathbf{t}^\perp. \quad (61)$$

The quantities with subscript 1 or 2 are associated with the pattern on the left or right side of the interface. For the continuous-director interface $\mathbf{n}_1 = \pm\mathbf{n}_2$, such as the examples in Fig. 5, the first term in (58) for the two patterns on the two sides of the interface will be canceled by the fact $\frac{d\phi_1}{dl} = \frac{d\phi_2}{dl}$. Then the integrated GC along a line is given by the integral of the perpendicular jumps of the bend and splay vectors:

$$(Continuous-director\ case:) \quad \Omega = \int K_A dA = \int (\lambda^{1+\nu} \Delta \mathbf{b}^\perp - \lambda^{-(1+\nu)} \Delta \mathbf{s}^\perp) dl. \quad (62)$$

The two examples in Fig. 5 have non-vanishing jumps of the bend and splay vectors across the interfaces by the formulae (57), (59) and (62), therefore, the resultant actuated interfaces bear non-zero GC for both cases. If a nematic defect falls exactly on the boundary (as seen, for example, in Fig. 5) it will generically generate an additional point like concentration of GC giving a tip in the resultant surface. In a Gauss-Bonnet loop around such a point, we cannot assume $\frac{d\phi_1}{dl} = \pm \frac{d\phi_2}{dl}$, as ϕ will jump along the defective side, and not along the regular side. The tip is generated by the corresponding singularity in $d\phi/dl$ on the defective side, and is thus not accounted for in our lineal densities of integrated curvature ((60) and (62)), which apply only where the lineal density is finite.

We comment here about the three distinct methods of calculating the concentrated GC along a crease. The first two methods are intrinsically equivalent in applying differential geometry to the explicit deformation that maps the reference domain on 2D to a 3D surface. The spiral pattern we study in this paper induces the explicit cone deformation so that the first two methods are applicable. But these two methods can not handle the concentrated GC along a crease on a general director pattern, because the explicit deformation is unknown. Then the formulae (60) and (62) derived from the metric are necessary. More importantly, the third method provides a possible way of considering a general crease and its concentrated GC on actuating a general director pattern. We reserve this point as a future work.

Remark. The formulae for the geodesic curvature and the concentrated Gaussian curvature are derived for LCE systems, which have a contraction factor λ along the director and an elongation factor $\lambda^{-\nu}$ along the perpendicular direction to the director. But these formulae for concentrated GC can be generalized to apply to any 2D contraction/elongation system, such as pneumatic (inflation) systems [43, 45, 44], swelling [50], and kirigami [25], by replacing λ and λ^ν with the metric-changing factors λ_{\parallel} and λ_{\perp} of the particular system. One should also notice that the interface has to be metric-compatible in these systems.

5.4 Concentrated GC for all types of metric-compatible interfaces

We derive the analytical forms of the concentrated GC for all types of the metric-compatible interfaces by the third method. We have confirmed that these formulae agree with those computed from the other methods. For hyperbolic-type and elliptic-type interfaces, we only provide the condensed but explicit formulae. For continuous-director interfaces and concentric spiral interfaces, the formulae are concise and obviously reveal the features of the GC.

Hyperbolic-type and elliptic-type interfaces. Recalling the hyperbolic-type interface $\mathbf{x}(u)$ in (22) and the GC (60) for the twinning case, the once(transverse)-integrated concentrated GC in terms of u is

$$\frac{d\Omega}{du} = \frac{2\lambda^{1-\nu}}{\mathbf{t} \cdot \mathbf{a} \cdot \mathbf{t}} \frac{d\phi}{du} + (\lambda^{1+\nu} \Delta \mathbf{b}^\perp - \lambda^{-1-\nu} \Delta \mathbf{s}^\perp) \frac{dl}{du}, \quad (63)$$

in which

$$\begin{aligned}
\mathbf{t}(u) &= \mathbf{x}'(u)/|\mathbf{x}'(u)|, \quad \phi(u) = \text{sign}(\mathbf{n}_1 \times \mathbf{t} \cdot \mathbf{e}_3) \arccos(\mathbf{n}_1 \cdot \mathbf{t}), \quad \frac{dl}{du} = |\mathbf{x}'(u)| = \frac{\sqrt{|\mathbf{r}_1||\mathbf{r}_2|}}{\cos \frac{\alpha_1 + \alpha_2}{2}}, \\
\Delta \mathbf{b}^\perp &= \left(\frac{\sin \alpha_1}{|\mathbf{r}_1|} \mathbf{n}_1^\perp - \frac{\sin \alpha_2}{|\mathbf{r}_2|} \mathbf{n}_2^\perp \right) \cdot \mathbf{t}^\perp, \quad \Delta \mathbf{s}^\perp = \left(\frac{\cos \alpha_1}{|\mathbf{r}_1|} \mathbf{n}_1 - \frac{\cos \alpha_2}{|\mathbf{r}_2|} \mathbf{n}_2 \right) \cdot \mathbf{t}^\perp, \\
\mathbf{r}_i &= \mathbf{x}(u) - \mathbf{c}_i, \quad \mathbf{n}_i = \mathbf{R}(\alpha_i) \frac{\mathbf{r}_i}{|\mathbf{r}_i|}, \quad \mathbf{n}_i^\perp = \mathbf{R}(\pi/2) \mathbf{n}_i, \quad \mathbf{t}^\perp = \mathbf{R}(\pi/2) \mathbf{t}, \\
\mathbf{a} &= \lambda^2 \mathbf{n}_1 \otimes \mathbf{n}_1 + \lambda^{-2\nu} \mathbf{n}_1^\perp \otimes \mathbf{n}_1^\perp,
\end{aligned} \tag{64}$$

where $i = 1, 2$ denotes the pattern on the left or the right side of the interface and $\mathbf{R}(\cdot)$ is a rotation in 2D. The Jacobean dl/du (dl/dv for elliptic-type interfaces) in (64) is directly calculated by taking the norm of the derivative of $\mathbf{x}(u)$ ($\mathbf{x}(v)$ for elliptic-type interfaces), and has the same form for both cases. The definition of $\phi(u)$ in (64) has encoded the counterclockwise rotation from \mathbf{n}_1 to \mathbf{t} . While the formula (63) is generically complicated, special choices of α_i and $\mathbf{x}(u)$ can simplify the expression. We provide one example in the next section showing the concise formula explicitly for the straight-line interface between two equal and opposite spiral patterns. The calculation for elliptic-type interfaces follows naturally by replacing $\mathbf{x}(u)$ with $\mathbf{x}(v)$ given in (25).

Continuous-director interfaces. For the horizontal interface $\mathbf{x}(l) = (l, 0), l \in \mathbb{R}$, in (33) with $\alpha_1 = \alpha_2$ or $\alpha_1 - \alpha_2 = \pm\pi$, we employ Eq. (62) to calculate the concentrated GC. The interface has a unit speed parameterisation and the arising Jacobean is unity. Recalling the formulae (57) and (59) for the bend and splay vectors, we have

$$\mathbf{b}_1 \cdot \mathbf{t}^\perp = \frac{\sin \alpha \cos \alpha}{l + c}, \quad \mathbf{b}_2 \cdot \mathbf{t}^\perp = \frac{\sin \alpha \cos \alpha}{l - c}, \quad \mathbf{s}_1 \cdot \mathbf{t}^\perp = \frac{\sin \alpha \cos \alpha}{l + c}, \quad \mathbf{s}_2 \cdot \mathbf{t}^\perp = \frac{\sin \alpha \cos \alpha}{l - c}. \tag{65}$$

Substituting the bend and splay vectors into Eq. (62) yields the analytical form of the concentrated GC as

$$\frac{d\Omega}{dl} = (\lambda^{1+\nu} - \lambda^{-1-\nu}) \frac{c \sin(2\alpha)}{c^2 - l^2}. \tag{66}$$

For the circular interface (35) with $\alpha_1 \neq \alpha_2$ and $\alpha_1 - \alpha_2 \neq \pm\pi$, we have the parametric form of the interface

$$\mathbf{x}(\theta) = (\bar{r} \cos \theta, c/\tan(\alpha_1 - \alpha_2) + \bar{r} \sin \theta) \tag{67}$$

where $\bar{r} = c/|\sin(\alpha_1 - \alpha_2)|$. We obtain the quantities for the GC in a way similar to (64), but with θ as the parametric parameter. By direct calculation, we have the concentrated GC variation with θ as

$$\frac{d\Omega}{d\theta} = -(\lambda^{1+\nu} - \lambda^{-1-\nu}) \frac{\cos(\alpha_1 + \alpha_2 - \theta) \sin(\alpha_1 - \alpha_2)}{2\sigma \cos(\alpha_1 - \alpha_2) + 2 \sin \theta}, \tag{68}$$

where $\sigma = \text{sign}(\sin(\alpha_1 - \alpha_2))$. The minus sign in front of the formula arises because the spiral pattern with α_2 (α_1) is on the left (right) side of the interface, not the other way which is common in the hyperbolic-type interface case in Fig. 4.

Note, quite counter-intuitively, director fields continuous at the interface can also yield non-vanishing, concentrated GC along lines, due to jumps in splay and bend.

Concentric spiral interface. Recall that the concentric spiral interface is given by

$$r(\theta) = r_0 \exp\left(\frac{\theta}{\tan \alpha}\right) \tag{69}$$

in polar coordinates, where $\alpha = \bar{\alpha} = (\alpha_1 + \alpha_2)/2$ or $\alpha = \bar{\alpha} + \pi/2$, and α_1 (α_2) is the spiral parameter for the pattern on the left (right) side of the interface satisfying $\alpha_1 + \alpha_2 \neq 0, \pm\pi$. See Eq. (38) and Fig. 6. The “side” of the interface is consistent with the interface tangent \mathbf{t} in terms of θ , i.e., $\mathbf{t} = [r_0 \exp(\frac{\theta}{\tan \alpha}) (\cos \theta, \sin \theta)]' / (dl/d\theta)$. For example, the vector $\mathbf{e}_3 \times \mathbf{t}$ points to the left side of the interface. The angle ϕ between the interface tangent and the director is constant, so the first term of (60) vanishes. Prior to calculating the GC, we have

$$\frac{dl}{d\theta} = \frac{r(\theta)}{|\sin \alpha|}, \quad \Delta \mathbf{b}^\perp = \Delta \mathbf{s}^\perp = \pm \frac{\sin(\alpha_1 - \alpha_2) \cos \alpha}{r(\theta)}, \quad (70)$$

where “+” corresponds to the case $\alpha = \bar{\alpha} = (\alpha_1 + \alpha_2)/2$ and “-” corresponds to the case $\alpha = (\alpha_1 + \alpha_2)/2 + \pi/2$. Then the concentrated GC in terms of θ is

$$\frac{d\Omega}{d\theta} = \pm(\lambda^{1+\nu} - \lambda^{-1-\nu}) \frac{\sin(\alpha_1 - \alpha_2) \cos \alpha}{|\sin \alpha|}. \quad (71)$$

The formula reveals that the concentrated GC of the spiral interface is a non-zero constant independent of θ . Although the length of a log spiral from $-\infty \rightarrow \theta$ is finite ($l = r(\theta) \sec \alpha$), the GC integrated along the crease diverges since the integrated GC per unit length along the crease diverges as $d\Omega/dl = \pm(\lambda^{1+\nu} - \lambda^{-1-\nu}) \sin(\alpha_1 - \alpha_2)/l$ on approaching the spiral center where $l = 0$, the length l in the problem determining the scale of geodesic curvature.

For the case $\alpha_1 + \alpha_2 = 0, \pm\pi$, the radial line interface $\mathbf{x}(r) = (r \cos \xi, r \sin \xi)$, $r \in [0, R]$ in Fig. 5(c), has the concentrated GC

$$\frac{d\Omega}{dr} = (\lambda^{1+\nu} - \lambda^{-1-\nu}) \frac{\sin(2\alpha_1)}{r} \quad (72)$$

by substituting

$$\Delta \mathbf{b}^\perp = \Delta \mathbf{s}^\perp = \frac{\cos \alpha_1 \sin \alpha_1}{r} - \frac{\cos \alpha_2 \sin \alpha_2}{r}. \quad (73)$$

Again, α_1 is chosen as the parameter for the spiral pattern on the left side of the interface. The circular interface in Fig. 5(d) bears no GC since it is on a developable cone surface.

5.5 Examples

We provide two examples of the analytical and simulated concentrated GC along creases for the twinning case and the continuous-director case. The twinning case in Fig. 10 consists of two spiral patterns with equal and opposite α s, that is $\alpha_1 = -\alpha_2$. The metric-compatible interface is a straight line passing through the bisector of the two patterns. The continuous-director case consists of two spiral patterns with $\alpha_1 = \alpha_2$. The interface is a horizontal line passing through the two spiral centers. The analytical formulae and plots of the concentrated GC for the two examples are obtained according to Eqs. (60) and (62). The results of simulations with the code Morphoshell qualitatively agree with the analytical solutions.

5.5.1 Theoretical and numerical results for the straight-line interface bisecting the two opposite spirals

We establish the coordinates in Fig. 10(a). The centers of the two spiral patterns with $\alpha = \alpha_1 = -\alpha_2$ are located at $(-c, 0)$ and $(c, 0)$. The interface is a vertical straight line passing through the bisector

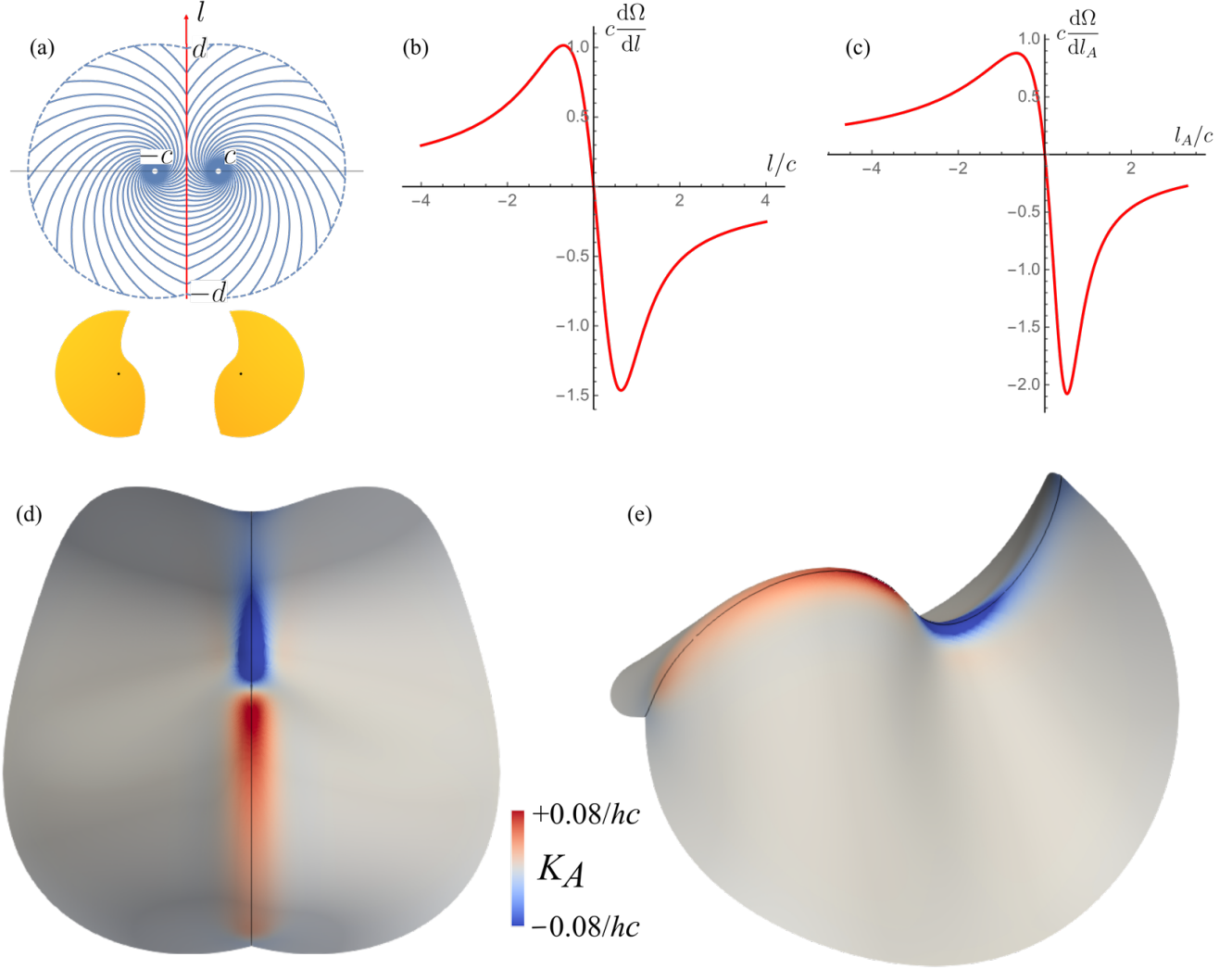


Figure 10: (a) The straight-line interface passing through the bisector between two spiral patterns with $\alpha_1 = -\alpha_2 = 1.25$, a special value for our λ where the actuation of an isolated pattern would be a flat state, but with rotations. There are no tips and hence no point sources of GC to obscure the crease contributions. (b) The non-dimensionalized concentrated GC $c d\Omega/dl$ has positive and negative regions along the non-dimensionalized position l/c in the reference interface. The positive (negative) GC is concentrated near the position $l \lesssim 0$ ($l \gtrsim 0$). (c) The plot of non-dimensionalized concentrated GC $c d\Omega/dl_A$ against the non-dimensionalized actuated arc length l_A/c . (d)-(e) The simulated GC rescaled by hc . The simulation shows the smearing out of the GC, which leads to the blunting of the theoretical interface indicated by the thin black line.

and ranging from $-d$ to d . The parameters we choose are $\alpha = \arctan(\lambda^{-\frac{1-\nu}{2}})$, $d = 2\sqrt{15}$ and $c = 2$, where the materials constants are $\lambda = 0.7$ and $\nu = 0.5$. This spiral constant α leads to a cone with cone angle $\varphi = \pi/2$, that is, the actuated configuration is in 2D with no cone tip, as illustrated in Fig. 10(a). We are thus able to dis-aggregate the localized tip and the crease contributions to the GC.

The quantities required in Eq. (55) for the left pattern are

$$\phi = \pi/2 - \alpha - \arctan(l/c), \quad b = \sin \alpha / \sqrt{c^2 + l^2}, \quad s = \cos \alpha / \sqrt{c^2 + l^2}. \quad (74)$$

Substituting ϕ , b and s into (55), one can obtain the geodesic curvature κ_{g_1} for the left pattern. A similar argument applies to the geodesic curvature κ_{g_2} of the right pattern. In fact, transforming $\alpha \rightarrow -\alpha$ and $\phi \rightarrow -\phi$ in (55) for the right pattern, we realize that $\kappa_{g_2} = -\kappa_{g_1}$. To calculate the concentrated GC per unit reference state length, $d\Omega/dl$, by (48) and (60), one has to multiply the geodesic curvature in (58) by the Jacobian $\sqrt{\lambda^2 \cos^2 \phi + \lambda^{-2\nu} \sin^2 \phi}$. Omitting calculation details, we provide the theoretical result for the concentrated GC for the given example as

$$\begin{aligned} \frac{d\Omega}{dl} &= 2 \frac{\lambda^{-1-\nu} \cos \alpha \sin \phi + \lambda^{1+\nu} \sin \alpha \cos \phi}{\sqrt{c^2 + l^2}} - \frac{2c}{(c^2 + l^2)(\lambda^{-1-\nu} \sin^2 \phi + \lambda^{1+\nu} \cos^2 \phi)} \\ &= 2(\lambda^{-1-\nu} s \sin \phi + \lambda^{1+\nu} b \cos \phi) - \frac{2c(s^2 + b^2)}{\lambda^{-1-\nu} \sin^2 \phi + \lambda^{1+\nu} \cos^2 \phi}, \end{aligned} \quad (75)$$

where ϕ , b and s are functions of l defined in (74). Figure 10(b) illustrates the non-dimensionalized concentrated GC $d\Omega/dl$ against the position l on the reference domain. One can observe that the concentrated GC has positive and negative regions, where the negative GC is concentrated near $l = 0$. To compare with the numerical simulation more illustratively, we provide another plot showing the concentrated GC against the arc length of the actuated crease in Fig. 10(c). The plot has features similar to the previous one. The simulation in Fig. 10 shows that the GC is ‘‘smeared out’’ over a neighborhood around the crease, indicating localized non-isometry and corresponding to the ‘‘blunting’’ effect discussed in Section 3. The trend of the value of GC (small positive \rightarrow large positive \rightarrow large negative \rightarrow small negative) shown in the simulation agrees with the analytical solution in Fig. 10(c). The localisation of non-isometry suggest that isometric deformations can be used to analyze the evolution of the surfaces outside the non-isometric neighborhood of the crease.

5.5.2 Theoretical and numerical results for the horizontal continuous-director interface

Establishing the coordinates in Fig. 11(a), the centers of the two equal spiral patterns with $\alpha = \alpha_1 = \alpha_2$ are at $(-c, 0)$ and $(c, 0)$. The interface is a horizontal line passing through the two centers, ranging from $-d$ to d . The parameters we choose for this example are $\alpha = 1.173$, $d = 8$ and $c = 2$.

Recalling the GC distribution (66) for the horizontal interface and, we have

$$\frac{d\Omega}{dl} = (\lambda^{1+\nu} - \lambda^{-1-\nu}) \frac{c \sin(2\alpha)}{c^2 - l^2}. \quad (76)$$

The plots of the non-dimensionalized, concentrated GC per unit length against the reference position l and the actuated arc length l_A are provided in Figs. 11(b) and (c) respectively. One can observe that the GC is positive for $l \in [-d, -c] \cup (c, d]$ and negative for $l \in (-c, c)$, and approaches positive infinity as $|l| \rightarrow c^+$, and negative infinity as $|l| \rightarrow c^-$. These features are consistent with the analytical form (76) with the chosen parameters. Note that the reference state calculation of geodesic curvature, Eq. (55), leading to (60), (62), and (76), does not contain the singular defect-like contributions from the activated tip regions.

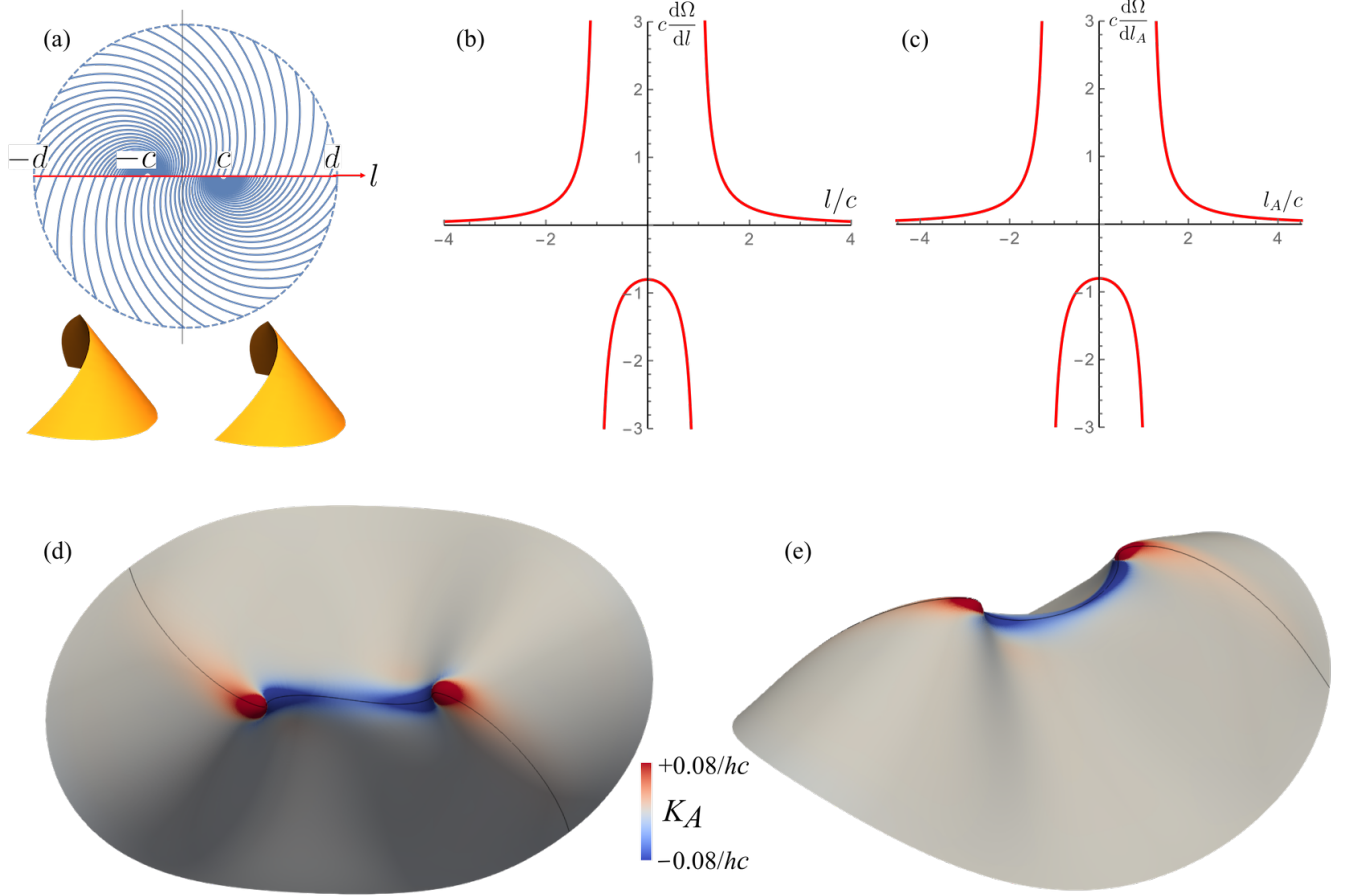


Figure 11: (a) The horizontal continuous-director interface between two spiral patterns with $\alpha_1 = \alpha_2 = 1.173$. We choose the parameters $l \in [-d, d]$, $d = 8$, along the horizontal axis to be consistent with the previous example. The spiral centers are at $(-c, 0)$ and $(c, 0)$ with $c = 2$. (b) The non-dimensionalized, concentrated GC $c d\Omega/dl$ has the positive region ($l \in [-d, -c) \cup (c, d]$) and negative region ($l \in (-c, c)$) along the non-dimensionalized position l/c of the reference interface. The GC approaches positive infinity as $l \rightarrow -c^-$ or $l \rightarrow c^+$, and negative infinity as $l \rightarrow -c^+$ or $l \rightarrow c^-$. (c) The plot of non-dimensionalized, concentrated GC $c d\Omega/dl_A$ against the non-dimensionalized, actuated arc length l_A/c has similar features. (d)–(e) The simulated GC rescaled by hc . The simulation shows the smearing out of the GC, leading to the blunted interface indicated by the thin black line.

Another interesting observation from (76) is that $d\Omega/dl = 0$ when $\alpha = \pm\pi/2$ and $l \neq \pm c$, which means the horizontal continuous-director interface between two circular patterns bears no GC, apart from that of the circle centers themselves. This discrepancy between the (lack of) concentrated GC in circular patterns and that for spiral patterns relies on the fact that the splay and bend are discontinuous across the interface only for spirals, not circles.

The simulation in Fig. 11 qualitatively agrees with the theoretical result and also shows the localisation of the smeared GC in a neighborhood of the crease. Integrating (76) from $-l$ to l (taking principal parts etc.), for $l > c$, gives $(\lambda^{1+\nu} - \lambda^{-1-\nu}) \sin(2\alpha) \ln [(l+c)/(l-c)]$ which vanishes

for large l . However, as mentioned earlier, this calculation does not account for the defect-like semi-tip contributions, which can be calculated as follows: In the far field of a split-spiral cone pattern such as in Fig. 11, one perceives just a single spiral cone whose integrated GC is $2\pi(1 - \sin \varphi)$. This quantity must therefore equal the total integrated GC arising from the split-spiral pattern, consistent with the vanishing of the integral of (76).

6 Discussion

One single spiral pattern evolves into a cone or an anticone with GC localized at its tip upon actuation. In this work, we have calculated all possible metric-compatible interfaces between two centers of GC, i.e., spiral patterns. By employing the metric compatibility equation and elliptic coordinates, we have found there are four, and only four, types of interfaces between spiral patterns: hyperbolic-type, elliptic-type, continuous-director, and concentric spiral interfaces. Since these interfaces are generically inconsistent under cone deformations, the deformed interfaces for each pattern are further isometrically or non-isometrically deformed in order to join one with the other continuously. The simulations suggest that the non-isometric deformation only occurs in a small neighborhood of the actuated interface, so as to trade the bending energy of the fold with the stretching energy, leading to blunted interface. Except for the non-isometric neighborhood, the rest of the surface exhibits nearly isometric evolution which further reduces the bending energy of the surfaces. This phenomenon has been observed numerically in a previous work [16].

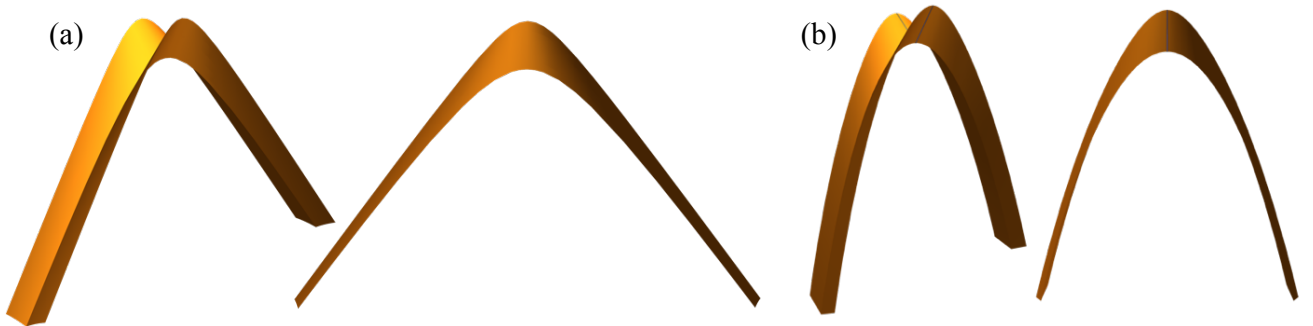


Figure 12: (a) The original fold is cut from the cone intersection in Fig. 1(b). (b) The relaxed fold is deformed isometrically from the original fold in (a). Two views are provided for each case to illustrate the curved creases.

Inspired by seminal prior work in isometric curved-fold origami [20, 13, 11], the geometrical evolution of the fold between cones can be further understood, assuming the non-isometric deformation is localized in the neighborhood of the fold. Figures 12(a) and (b) sketch the evolution of LCE folds between two cones. The original fold in Fig. 12(a) is constructed by cutting off a narrow strip that contains the fold between two cones and isolated from the point defects of the concentrated GC, i.e., the tips. The relaxed fold in Fig. 12 is deformed isometrically from the original one. Following results from differential geometry [20], the opening angle of the fold is determined by the total curvature and the geodesic curvature of the curved crease. For the isometric origami case, the opening angle is symmetric with respect to the crease by the fact that the geodesic curvatures from the two

sides are identical. But for the non-isometric case, the opening angle is generically asymmetric, and is potentially programmable by programming the geodesic curvature.

On the mechanics front, determining the final state of a non-isometric curved-fold strip is essentially an energy minimization problem. Without stretching, the total elastic energy E_{total} of the folded strip with developable facets is given by a simplified model [13, 26] with contributions from the bending energy E_b and the energy of the crease E_c :

$$E_{total} = E_b + E_c = \frac{1}{2}D \int (2H)^2 dA_A + \frac{1}{2}K \int (\theta(l_A) - \theta_0(l_A))^2 dl_A, \quad (77)$$

where D is the bending modulus, K is the crease stiffness, H is the mean curvature distributed over the union of the two developable surfaces with area A_A , the arc length of the actuated crease is l_A , and $\theta(l_A)$ is the opening angle of the crease which is assumed to be close to the rest angle $\theta_0(l_A)$. The bending energy, i.e. the first term of (77), is usually treated as the Wunderlich functional [49, 12] by integrating along the generator of the surface first and then lowering the integral to one dimension along the curved crease. The bending energy is divergent when the surface has point defects (e.g. cone tips) [47, 56]. The rest angle $\theta_0(l_A)$ is usually treated as a constant angle in isometric origami [13, 26], but is expected to vary with the arc length in the non-isometric origami case because of the concentrated GC.

Unlike isometric folds, non-isometric folds are not Gaussian flat, so their evolution is constrained by the non-zero GC. For example, one can not unfold it onto the 2D plane without stretching. The stretching energy will emerge when deforming the folded strip beyond the threshold of isometric deformation. In other words, the concentrated GC will lead to a stronger folded strip by preventing it from entering the stretching regime. Moreover, as mentioned above, a general director field does not result in a developable surface necessarily. Though the metric-compatible interface between general director patterns still exists, determining the actuated state consisting of curved interface and non-developable surfaces is challenging because of the coupling of the stretch, bend, and geometry. According to these discussions, we propose several interesting questions for the future study:

- What is the physically relevant model for the energy of a crease bearing non-vanishing GC?
- Can we program the geodesic curvature of the crease and the distribution of point defects to inverse design a non-isometric folded strip that can approximate a target curve in space?
- Can we have a theory for the mechanics of a non-isometric folded strip with two non-developable side surfaces and a curved crease deformed from a general director pattern?

Understanding all these questions is useful for LCE engineering applications such as designing new LCE actuators, lifters, and robotics.

Acknowledgements

F.F. and M.W. were supported by the EPSRC [grant number EP/P034616/1]. D.D. was supported by the EPSRC Centre for Doctoral Training in Computational Methods for Materials Science [grant no. EP/L015552/1]. J.S.B. was supported by a UKRI “future leaders fellowship” [grant number MR/S017186/1].

Authors' Contributions

F.F., J.S.B. and M.W. performed the theoretical calculations. D.D. performed all the simulations. D.D and J.S.B. developed the simulation platform.

References

- [1] H. Aharoni, E. Sharon, and R. Kupferman. Geometry of thin nematic elastomer sheets. *Physical Review Letters*, 113(25):257801, 2014.
- [2] H. Aharoni, Y. Xia, X. Zhang, R. D. Kamien, and S. Yang. Universal inverse design of surfaces with thin nematic elastomer sheets. *Proceedings of the National Academy of Sciences*, 115(28):7206–7211, 2018.
- [3] B. Audoly and Y. Pomeau. *Elasticity and geometry: from hair curls to the non-linear response of shells*. Oxford university press, 2010.
- [4] N. P. Bende, A. A. Evans, S. Innes-Gold, L. A. Marin, I. Cohen, R. C. Hayward, and C. D. Santangelo. Geometrically controlled snapping transitions in shells with curved creases. *Proceedings of the National Academy of Sciences*, 112(36):11175–11180, 2015.
- [5] K. Bhattacharya. *Microstructure of Martensite: Why it forms and how it gives rise to the shape-memory effect*, volume 2, Oxford Series on Materials Modelling. Oxford University Press, 2003.
- [6] S. J. Callens and A. A. Zadpoor. From flat sheets to curved geometries: Origami and kirigami approaches. *Materials Today*, 21(3):241–264, 2018.
- [7] G. P. Choi, L. H. Dudte, and L. Mahadevan. Programming shape using kirigami tessellations. *Nature materials*, 18(9):999–1004, 2019.
- [8] J. Choma. Paper folding to foldable composites. In *Acadia 2019: Ubiquity and Autonomy: Project Catalog of the 39th Annual Conference of the Association for Computer Aided Design in Architectur*, page 80–85. ACADIA Publishing Company, 2019.
- [9] X. Dang, F. Feng, P. Plucinsky, R. D. James, H. Duan, and J. Wang. Inverse design of deployable origami structures that approximate a general surface. *arXiv preprint arXiv:2008.02349*, 2020.
- [10] E. D. Demaine, M. L. Demaine, and D. Koschitz. Reconstructing David Huffman’s legacy in curved-crease folding. In *Origami 5: Fifth International Meeting of Origami Science, Mathematics, and Education*, page 39. Taylor & Francis Group, 2011.
- [11] M. A. Dias and B. Audoly. A non-linear rod model for folded elastic strips. *Journal of the Mechanics and Physics of Solids*, 62:57 – 80, 2014. Sixtieth anniversary issue in honor of Professor Rodney Hill.

- [12] M. A. Dias and B. Audoly. “Wunderlich, meet Kirchhoff”: A general and unified description of elastic ribbons and thin rods. In *The Mechanics of Ribbons and Möbius Bands*, pages 49–66. Springer, 2016.
- [13] M. A. Dias, L. H. Dudte, L. Mahadevan, and C. D. Santangelo. Geometric mechanics of curved crease origami. *Physical review letters*, 109(11):114301, 2012.
- [14] L. H. Dudte, E. Vouga, T. Tachi, and L. Mahadevan. Programming curvature using origami tessellations. *Nature materials*, 15(5):583–588, 2016.
- [15] D. Duffy and J. S. Biggins. Defective nematogenesis: Gauss curvature in programmable shape-responsive sheets with topological defects. *Soft Matter*, 16:10935–10945, 2020.
- [16] D. Duffy, L. Cmok, J. S. Biggins, A. Krishna, C. D. Modes, M. K. Abdelrahman, M. Javed, T. H. Ware, F. Feng, and M. Warner. Shape programming lines of concentrated Gaussian curvature. *arXiv preprint arXiv:2101.07041*, 2021.
- [17] J. P. Duncan and J. Duncan. Folded developables. *Proceedings of the Royal Society of London. A. Mathematical and Physical Sciences*, 383(1784):191–205, 1982.
- [18] F. Feng, J. S. Biggins, and M. Warner. Evolving, complex topography from combining centers of Gaussian curvature. *Phys. Rev. E*, 102:013003, Jul 2020.
- [19] F. Feng, P. Plucinsky, and R. D. James. Phase transformations and compatibility in helical structures. *Journal of the Mechanics and Physics of Solids*, 131:74–95, 2019.
- [20] D. Fuchs and S. Tabachnikov. More on paperfolding. *The American Mathematical Monthly*, 106(1):27–35, 1999.
- [21] Y. Ganor, T. Dumitrică, F. Feng, and R. D. James. Zig-zag twins and helical phase transformations. *Philosophical Transactions of the Royal Society A: Mathematical, Physical and Engineering Sciences*, 374(2066):20150208, 2016.
- [22] C. F. Gauss. *Disquisitiones generales circa superficies curvas*, volume 1. Typis Dieterichianis, 1828.
- [23] I. Griniasty, H. Aharoni, and E. Efrati. Curved geometries from planar director fields: Solving the two-dimensional inverse problem. *Physical review letters*, 123(12):127801, 2019.
- [24] C. Jiang, K. Mundilova, F. Rist, J. Wallner, and H. Pottmann. Curve-pleated structures. *ACM Transactions on Graphics (TOG)*, 38(6):1–13, 2019.
- [25] L. Jin, A. E. Forte, B. Deng, A. Rafsanjani, and K. Bertoldi. Kirigami-inspired inflatables with programmable shapes. *Advanced Materials*, 32(33):2001863, 2020.
- [26] T. Jules, F. Lechenault, and M. Adda-Bedia. Local mechanical description of an elastic fold. *Soft Matter*, 15(7):1619–1626, 2019.
- [27] J. Kim, J. A. Hanna, R. C. Hayward, and C. D. Santangelo. Thermally responsive rolling of thin gel strips with discrete variations in swelling. *Soft Matter*, 8(8):2375–2381, 2012.

- [28] Y. Klein, E. Efrati, and E. Sharon. Shaping of elastic sheets by prescription of non-euclidean metrics. *Science*, 315(5815):1116–1120, 2007.
- [29] K. Kuribayashi, K. Tsuchiya, Z. You, D. Tomus, M. Umemoto, T. Ito, and M. Sasaki. Self-deployable origami stent grafts as a biomedical application of Ni-rich TiNi shape memory alloy foil. *Materials Science and Engineering: A*, 419(1-2):131–137, 2006.
- [30] C. Modes, K. Bhattacharya, and M. Warner. Gaussian curvature from flat elastica sheets. *Proceedings of the Royal Society A: Mathematical, Physical and Engineering Sciences*, 467(2128):1121–1140, 2011.
- [31] C. D. Modes and M. Warner. Blueprinting nematic glass: Systematically constructing and combining active points of curvature for emergent morphology. *Physical Review E*, 84(2):021711, 2011.
- [32] C. D. Modes and M. Warner. The activated morphology of grain boundaries in nematic solid sheets. In *Emerging Liquid Crystal Technologies VII*, volume 8279, page 82790Q. International Society for Optics and Photonics, 2012.
- [33] C. D. Modes and M. Warner. Negative Gaussian curvature from induced metric changes. *Physical Review E*, 92(1):010401, 2015.
- [34] C. Mostajeran. Curvature generation in nematic surfaces. *Phys. Rev. E*, 91:062405, Jun 2015.
- [35] C. Mostajeran, M. Warner, and C. D. Modes. Frame, metric and geodesic evolution in shape-changing nematic shells. *Soft matter*, 13(46):8858–8863, 2017.
- [36] C. Mostajeran, M. Warner, T. H. Ware, and T. J. White. Encoding Gaussian curvature in glassy and elastomeric liquid crystal solids. *Proceedings of the Royal Society A: Mathematical, Physical and Engineering Sciences*, 472(2189):20160112, 2016.
- [37] I. Niv and E. Efrati. Geometric frustration and compatibility conditions for two-dimensional director fields. *Soft matter*, 14(3):424–431, 2018.
- [38] B. O’Neill. *Elementary differential geometry*. Academic press, 2014.
- [39] S. Pellegrino. *Deployable structures*, volume 412. Springer, 2014.
- [40] P. Plucinsky, B. A. Kowalski, T. J. White, and K. Bhattacharya. Patterning nonisometric origami in nematic elastomer sheets. *Soft Matter*, 14:3127–3134, 2018.
- [41] P. Plucinsky, M. Lemm, and K. Bhattacharya. Programming complex shapes in thin nematic elastomer and glass sheets. *Physical Review E*, 94(1):010701, 2016.
- [42] K. A. Seffen. Spherical images and inextensible curved folding. *Physical Review E*, 97(2):023004, 2018.
- [43] E. Siéfert, E. Reyssat, J. Bico, and B. Roman. Bio-inspired pneumatic shape-morphing elastomers. *Nature materials*, 18(1):24–28, 2019.

- [44] E. Siéfert, E. Reyssat, J. Bico, and B. Roman. Programming stiff inflatable shells from planar patterned fabrics. *Soft Matter*, 16(34):7898–7903, 2020.
- [45] E. Siéfert and M. Warner. Inflationary routes to Gaussian curved topography. *Proceedings of the Royal Society A*, 476(2240):20200047, 2020.
- [46] Y. Song, X. Chen, V. Dabade, T. W. Shield, and R. D. James. Enhanced reversibility and unusual microstructure of a phase-transforming material. *Nature*, 502(7469):85–88, 2013.
- [47] E. Starostin and G. Van Der Heijden. The shape of a Möbius strip. *Nature materials*, 6(8):563–567, 2007.
- [48] T. Tachi. Generalization of rigid-foldable quadrilateral-mesh origami. *Journal of the International Association for Shell and Spatial Structures*, 50(3):173–179, 2009.
- [49] R. E. Todres. Translation of W. Wunderlich’s “on a developable Möbius band”. In *The Mechanics of Ribbons and Möbius Bands*, pages 23–34. Springer, 2016.
- [50] W. M. van Rees, E. A. Matsumoto, A. S. Gladman, J. A. Lewis, and L. Mahadevan. Mechanics of biomimetic 4d printed structures. *Soft matter*, 14(43):8771–8779, 2018.
- [51] T. H. Ware, M. E. McConney, J. J. Wie, V. P. Tondiglia, and T. J. White. Voxelated liquid crystal elastomers. *Science*, 347(6225):982–984, 2015.
- [52] M. Warner. Topographic mechanics and applications of liquid crystalline solids. *Annual Review of Condensed Matter Physics*, 11:125–145, 2020.
- [53] M. Warner and C. Mostajeran. Nematic director fields and topographies of solid shells of revolution. *Proceedings of the Royal Society A: Mathematical, Physical and Engineering Sciences*, 474(2210):20170566, 2018.
- [54] M. Warner and E. M. Terentjev. *Liquid crystal elastomers*, volume 120. Oxford university press, 2007.
- [55] T. J. White and D. J. Broer. Programmable and adaptive mechanics with liquid crystal polymer networks and elastomers. *Nature materials*, 14(11):1087–1098, 2015.
- [56] T. Yu, I. Andrade-Silva, M. A. Dias, and J. A. Hanna. Cutting holes in bistable folds. *Mechanics Research Communications*, page 103700, 2021.